NORTHWESTERN UNIVERSITY

Transmission Electron Microscopy Studies of Surface Phenomena in Polar Oxides

A DISSERTATION

SUBMITTED TO THE GRADUATE SCHOOL
IN PARTIAL FULFILLMENT OF THE REQUIREMENTS

for the degree

DOCTOR OF PHILOSOPHY

Field of Materials Science and Engineering

By

Arun Kumar Subramanian

EVANSTON, ILLINOIS

June 2005

ABSTRACT

Transmission Electron Microscopy Studies of Surface Phenomena in Polar Oxides

Arun Kumar Subramanian

Atomic scale processes at surfaces dictate the macroscopic properties of solid surfaces and have been the subject of numerous theoretical and experimental studies. Polar surfaces, due to their non-vanishing dipole moment along the surface normal, are unstable from classic electrostatics arguments. The ionic model often used to describe this class of materials falls short in explaining the experimental observations of stable polar surfaces. A change in the electronic structure of the surface has been proposed as a stabilization mechanism, but until this study has not been experimentally verified. The research approach described in this manuscript involves a combination of computational (Direct Methods) and experimental (TEM) methods for investigation of polar oxide surface structures. The results from the studies of the surfaces of three different polar oxides, namely MgO (111), NiO (111) and $SrTiO_3$ (110), are presented in this dissertation. The atomic structure and

charge density of the MgO (111)-$\sqrt{3}$x$\sqrt{3}$R30° reconstruction has been experimentally measured and verified by *ab initio* calculations. The structure and densities of two other reconstructions on the NiO (111) surface, namely the ($\sqrt{3}$x$\sqrt{3}$R30°) and (2x2), are also presented. The phase transition between these two surface phases of NiO is accompanied by a novel step ordering pheneomenon is documented using TEM and SEM. Finally, the results from the studies of the atomic struture of the $SrTiO_3$ (110)-3x4 surface reveal similarities with another surface structure ($SrTiO_3$ (100)-c(6x2)).

Approved by

Professor Laurence D. Marks

Department of Materials Science and Engineering

Northwestern University, Evanston, IL 60201, USA

Acknowledgements

First, I would like to thank my dissertation advisor, Prof. L. D. Marks for giving me the opportunity to work with him and for his patience during my learning process.

The opportunity of working in a group with state-of-the-art experimental hardware is a mixed blessing. The potential to do wonderful science (when things work) is an aspiration that drives one to endure the privations of getting things to work. In this context, I would like to offer my sincere gratitude to Dr. Daniel Grozea and Dr. Edy Widjaja for helping me through my crusades with SPEAR. Without their support and encouragement, I doubt if I could have made it this far.

I would like to thank the members of the Marksgroup - Csown, Yingmin, Ann, Arno, Courtney, Peter, & Brian and my classmates at Northwestern - Duane and Stephan, for enriching my life with interesting experiences during my graduate tenure at Northwestern. Special thanks are due to Hitachi engineer Ken Eberly for his timely help in dealing with problems in the lab, especially ones not related to the UHV-H9000.

I would also like to formally credit the following contribtions to this work: The DFT calculations presented in Chapter 3 of this manuscript were performed by

Dr. O. Warschkow and Prof. P. Blaha and those in Chapter 4 were carried out by Prof L. D. Marks. I am indebted to Dr. Karl Merkle of Argonne National Labs for providing the NiO single crystals used in this study.

And finally, this research project was supported by the National Science Foundation (grant number DMR-007-5834) whose support is gratefully acknowledged.

Contents

List of Tables

List of Figures

CHAPTER 1

Introduction

1.1. Why Surfaces?

Atomic scale processes at surfaces dictate the macroscopic properties of solid surfaces and have been the subject of numerous theoretical and experimental studies. A surface is the boundary between the bulk solid and its environment, and represents a rather unique type of defect in the solid state. At a surface, the periodicity of the bulk solid is abruptly terminated along one dimension which results in dangling bonds that increase the surface free energy. Under suitable conditions these atoms can relax and/or organize themselves into structures that have translational periodicities larger than those of bulk. This is more evident on low index surfaces since they have higher dangling bond densities. These reconstructions generally involve a few atomic layers and are accompanied by strain fields that decay exponentially into the bulk (Keating, 1966; Robinson et al., 1988). Reconstructions can be broadly divided into two classes: native and adatom induced, depending on the presence or absence of foreign species on the surface. Surface structures are classified by one of the 17 crystallographic plane groups since they possess only two-dimensional periodicity. The 2-D surface mesh generated by bulk truncation is the most natural co-ordinate system to describe the structure, and

the reconstruction is described by its size and orientation relative to the primitive 1x1 lattice (Marks et al., 1998). The conventional approach is to use the large unit cell since the reciprocal lattice points would then have integral indices.

The technological importance of surfaces and the various novel structures they adopt cannot be overstated. The semiconductor industry, with its ever shrinking device dimensions, drives the need for understanding the various atomic-scale surface phenomena. As the feature sizes in CMOS devices shrink, a transition needs to be made from the current microelectronics technology to moletronics (or molecular electronics) (Seminario et al., 2004a,b). In this limit, a bottom-up approach to device fabrication is inevitable, wherein devices are assembled a few atoms at a time. Nano-structured surfaces are used more and more nowadays as substrates for growing artificial structures with specific conformations. Reconstructed surfaces with large unit cells may also drive specific growth modes, favouring for example the formation of size-controlled clusters. Vicinal surfaces, which exhibit arrays of parallel steps, can be used to make quantum wires: the migration of metallic adatoms on the surface after deposition is driven by the presence of the steps, and the atoms gather in linear chains rather than disperse on the surface.

Another discipline where a fundamental understanding of surface processes is indispensable is catalysis. Traditionally, technological developments in the area of heterogeneous catalysis are products of the trial and error technique, though, research over the last few decades has shed some light on the underlying processes (Sinfelt, 1986). Vital to the understanding of a catalytic reaction is the knowledge

of the atomic-scale structure of the surface, which aids the identification of catalytically active sites. Oxides (of transition metals) comprise the vast majority of the catalysts used in the chemical industry, either in the form of the active material or as support. Transition metal cations exhibit multiple valencies and form a rich array of compounds whose bulk properties are well characterized (Johnson, 1982; Sorensen, 1981; Hamnett and Goodenough, 1984). The body of work in literature on the atomic and electronic properties of the surfaces of these materials was condensed into a book *Surface Science of Oxide Surfaces* by Henrich and Cox (1994). The more recent studies employing Scanning Tunneling microscopy/Atomic Force Microscopy (Freund et al., 1996), Grazing Incidence X-ray Diffraction (Renaud, 1998), Scanning Tunneling Spectroscopy (Bonnell, 1998) summarize the newer results. Despite extensive experimental and theoretical effort expended on this topic, a firm grasp of the underlying principles is still elusive.

A certain subset of surfaces in ionic solids , polar surfaces, merit special attention. From classical electrostatics, the stability of a compound surface depends on the characteristics of the charge distribution in the structural units repeating along the surface normal. Fig. 1.1 illustrates the various possible atomic configurations in this regard. Type 1 or Type 2 surfaces which differ in the charge Q borne by their layers have a zero dipole moment in their repeat unit and are thus potentially stable. In contrast, polar Type 3 surfaces have a diverging electrostatic surface energy (Tasker, 1979) due to the presence of a non-zero dipole moment not only on the outer layers (which would not distinguish them from non-polar

rumpled or reconstructed surfaces), but also on all the repeat units throughout the material. The cancellation of this macroscopic dipole moment can be achieved by one of three mechanisms:

(1) Changes in the stoichiometry of surface - Assuming that surface species retain their bulk oxidation states, the excess charge at the surface can be balanced by having a surface that is stoichiometrically different from the bulk. This process is usually accompanied by a reconstruction of the first few surface layers and faceting depending upon how the vacancies or adatoms order.

(2) Adsorption of charged foreign species - The residual atmosphere in the experimental set-up usually contains charged radicals, for example OH^-, which can adsorb on the surface and provide charge compensation.

(3) Modification of the surface electronic structure - Charge compensation can be attained through an electron redistribution in response to the polar electrostatic field. This is achieved by a total or partial filling of surface states , sometimes leading to surface metallization.

Polar surfaces of compound semiconductors have been studied extensively due to the fact that the (100) surface of zinc-blende compounds serves as a substrate for the growth of nearly all III–V and II–VI device layers. Pashley (Pashley, 1989) proposed an "electron-counting model" to explain the stability of such surfaces.

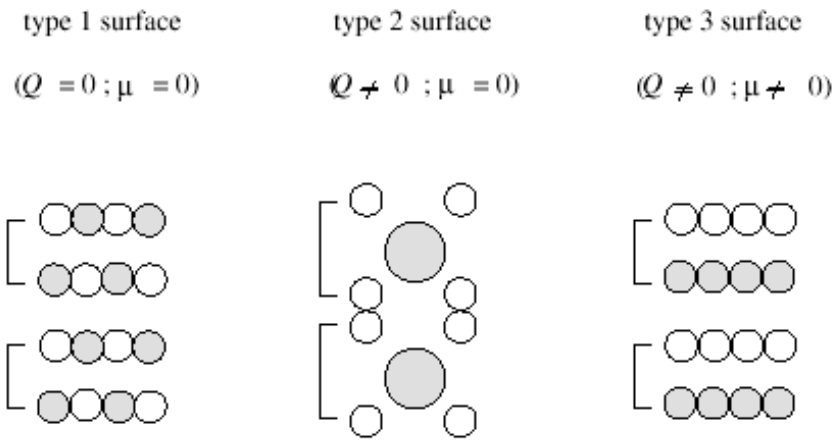

Figure 1.1. Classification of surfaces of compounds. Q is the total charge in a layer and $\vec{\mu}$ is the net dipole moment normal to the surface

The fundamental premise of the model is that the dangling bonds on the electropositive element are empty and those on the electronegative element are full. This condition necessarily results in a charge neutral surface and was successfully used to explain the atomic structure and surface step morphology of GaAs (001) and ZnSe (001) surfaces. However, this model has limited applicability and when applied does not uniquely determine the surface reconstruction.

Polar oxide surfaces are much more diverse, presenting a vast number of crystallographic structures: rock-salt, corundum, spinel, inverse spinel, wurtzite, perovskite. The nature of metal-oxygen bonding in these oxides span the entire range between fully ionic and primarily covalent. Transition metal oxides add another dimension to the problem forming mixed valence compounds (like Fe_3O_4) which

stabilize oxides with different stoichiometries depending on temperature and oxygen partial pressure. In a seminal article in 1992, Wolf (1992) argued that surfaces of ionic rock-salt oxides should be terminated with complete $(MO)_4$ octopolar units. The octopolar units ensure charge neutrality of the surface and also have rapidly decaying electrostatic interactions. However, this result is valid only if both the anion and the cation retain their bulk oxidation states and the surface reconstructs stoichiometrically. Since the atoms in the near surface region are in a very different environment (compared to bulk) they almost never have the same oxidation state as the bulk atoms. Also, the validity of this model in the presence of excess anions (or cations) is not clear. Nevertheless, the octopolar unit is a recurring structural motif in various reconstructions on MgO (111) (Subramanian et al., 2004), NiO (111) (Subramanian and Marks, 2005) and $SrTiO_3$ (111) surfaces (Chiaramonti, 2004). More recently, Warschkow et al. (2004) have hypothesized that the ability of the surface oxygen atoms to relax out of the surface plane can be used as a reliable predictor for determining the stability of various structures on $SrTiO_3$ (100) surface .

Despite these efforts, presently there is no definitive method of predicting what the surface rearrangements will be in a given material. Even the various atomic structures experimentally determined are in disagreement with theory in terms of energetics. They may well be kinetically trapped structures (Duke, 1996), but such discord helps in gaining significant insight into the nature of surfaces and help in developing a tool to predict surface structures.

1.2. Surface Characterization Techniques

Studies of surface structure date back to the 1960s and since then a myriad of techniques have been employed to probe the nature of surfaces. These can be broadly divided into two categories: electron probe and photon probe techniques. Electron probe techniques such as transmission electron microscopy (TEM), scanning transmission electron microscopy (STEM), reflection electron microscopy (REM), low energy electron microscopy (LEEM), etc. provide real space information at various resolutions while diffraction techniques like grazing incidence x-ray diffraction (GIXRD), transmission electron diffraction (TED), low energy electron diffraction (LEED), reflection high energy electron diffraction (RHEED) provide fourier space information. In addition to the techniques listed above, various spectroscopic techniques are available to detect the chemical composition and electronic structure of the surface such as x-ray photoelectron spectroscopy (XPS), reflection electron energy loss spectroscopy and auger electron spectroscopy (AES). These techniques differ in geometry, resolution, sensitivity and the nature of the information derived. Among the electron probe techniques, the resolution obtainable in REM and LEEM is insufficient at present to resolve the atomic structure of the surfaces. RHEED is very sensitive to displacements normal to the surface and is primarily used as a tool to detect the surface topography in modern molecular beam epitaxy (MBE) systems. LEED suffers heavily from multiple scattering effects that require detailed calculation. The weak nature

of the interaction of x-rays with matter coupled with the low signal levels from surface makes conventional XRD a non-feasible technique for surface structure analysis. The advent of bright synchrotron sources and the use of grazing incidence has revived GIXRD as a viable surface characterization tool. The various scanning probe techniques like scanning tunneling microscopy (STM) and atomic force microscopy (AFM) probe only the outermost layer and hence do not provide the complete picture. Also STM studies are limited to conducting samples since the electrons have to tunnel between the tip and the sample. A brief comparison of the various techniques is presented in Table. 1.1.

The primary tools used in the present study of surface reconstructions are TEM/TED techniques, although SEM and AFM were also employed in part. The biggest advantage of using a TEM rests on the fact that real and reciprocal space information can be procured simuntaneously at various length scales. Electron diffraction in transmission geometry has low signal levels since the signal essentially originates from a few atomic layers and is further attenuated by the scattering from bulk. Radiation damage due to high incident beam energies is another cause of concern and has been observed in the Au-Si(111)-5x2 surface (Marks and Plass, 1995) and in other multiple-valence transition metal oxides (Buckett, 1991). Despite these limitations, TEM/TED has emerged as a powerful tool for surface crystallography. The simplest and in many cases most powerful approach for studying surfaces is diffraction. Surface structures with periodicities different from the bulk give rise to weak superstructure spots in TED patterns. When the beam is along

Table 1.1. Comparison of various surface science techniques

Technique	Surface/Bulk Sensitivity	Data Collection mode	Nature of Information	Lateral Resolution
STM/STS	good/poor	serial	real space atomic and electronic structure	$\approx 1\mathring{A}$
GIXRD	good/poor	serial	fourier space atomic structure	$\leq 0.1\mathring{A}$
LEEM	good/good	parallel	real space structure	50-80 $\mathring{A}$
LEED	good/good	parallel	fourier space structure	$\leq 0.1\mathring{A}$
RHEED/REM	good/poor	parallel	fourier/real space structure	5-10 $\mathring{A}$
TEM	good/good	parallel	real space structure	1-2 $\mathring{A}$
TED	good/good	parallel	fourier space structure	$\leq 0.1\mathring{A}$
XPS/AES	good/poor	serial	surface electronic structure	200 $\mathring{A}$

the zone axis the intensities of these spots are complicated by the plasmon scattering around strong bulk spots. However tilting to an off-zone condition attenuates the bulk spots more than the surface spots thereby improving signal to noise ratio (Xu and Marks, 1992). This is due to the fact that the superstructure spots are 'relrods' along the surface normal in reciprocal space. With care, the intensities of these spots can be treated within the kinematical approximation (Tanishiro and Takayanagi, 1989; Twesten and Gibson, 1994). However, with the phase problem for surfaces, there is the additional complication of incomplete data sets since surface reflections periodically overlap with the bulk reflections and hence cannot be measured. Robust phasing algorithms, collectively called Direct Methods, were developed in the L. D. Marks research group at Northwestern for dealing with surface diffraction data(both electron and x-ray) (Sinkler and Marks, 1999; Marks et al., 2001a). These have been employed with great success to solve the atomic structures of a variety of surface reconstructions on elemental (Collazo-Davila et al., 1998a,b) and compound semiconductors (Kumpf et al., 2001a,b) as well as those of oxides (Erdman et al., 2002, 2003).

The objective of the presented work is to study the atomic and electronic structures of polar surfaces of oxides using transmission electron microscopy and computational techniques. These can then be used to enhance the present understanding of the stability of polar surfaces and also determine rules for predicting surface structures. Three oxide systems are considered in this study - MgO, NiO

and $SrTiO_3$ - each treated under different environmental conditions to stabilize different recosntructions. The former two are binary rock salt oxides and the latter is representative mixed metal oxide. In the following chapters the experimental approach is outlined (Chapter 2) with the results from MgO (111) in Chapter 3, NiO (111) in Chapter 4, $SrTiO_3$ (110) in Chapter 5. The conclusions and unresolved issues in the present work are described in Chapter 6 along with suggestions for future work.

CHAPTER 2

Experimental and Computational Techniques

This chapter outlines the various experimental and computational tools employed in the present study. In most surfaces, significant changes from "bulk" positions are limited to few layers at the top, but there are small perturbations in the positions of atoms in the layers below due to the accompanying strain (Robinson et al., 1988). TEM/TED is a powerful tool to study these structures since it probes both the top and the bottom surfaces of the sample in addition to the bulk material in between. In contrast, scanning probe techniques such as STM and AFM are sensitive only to the outermost layer (Hofer et al., 2001; Nakamura et al., 2001). Another important factor that must be borne in mind while studying surfaces is the cleanliness of the system employed for the study. For proper characterization of surface properties at the atomic scale the surface composition should remain essentially constant during the course of data acquisition. This mandates that the rate of adsorption of foreign species on the surface of interest must be minimized. At a pressure of 10^{-6} torr, the time it takes to cover the surface with a monolayer of gas molecules from ambient is about 1 second (assuming a sticking probablility of 1) (Chung, 2001). Typical observation time-frames are on the order of a few hours and to maintain a clean surface for this period the pressure

in the system should be better than 10^{-10} torr. Some semiconductor surface reconstructions, namely Si (111)-7x7 and Si (100)-2x1, are known to deconstruct due to reactions with the residual gases in high vacuum systems (Jayaram, 1995). Even oxide surfaces reconstructions that are stable at air, sometimes for months (Gajdardziska-Josifovska et al., 1991), may be susceptible to active species like atomic hydrogen created under the electron beam in a standard TEM. A UHV-TEM is thus a necessary tool for the study of surface phenomena irrespective of the material system.

2.1. UHV microscope and SPEAR

The UHV microscope and SPEAR system (Collazo-Davila et al., 1995) are pivotal to the research work described in this thesis. The UHV microscope is based around the Hitachi H-9000 transmission electron microscope, which was redesigned to be fully UHV compatible and bakeable to 200°C (Marks et al., 1988). In addition to standard electron microscopy, the instrument is equipped with a Gatan Parallel Electron Energy Loss Spectrometer which can be used for elemental analysis and determining sample thicknesses. A new 1024x1024 slow-scan CCD camera was retrofitted to the microscope, thus enabling real time digital imaging.

A UHV microscope is of little value unless it is interfaced to an *in situ* sample preparation system. The SPEAR system attached to UHV-H9000 is a state-of-the-art surface analysis system which has been used for studying a variety of materials (Grozea et al., 2000; Bengu and Marks, 2001; Widjaja and Marks, 2003; Erdman

et al., 2002). It consists of a transfer chamber, a central carousel for moving TEM samples to various side ports. Currently, there are four sidechambers:

(1) SINBAD, which is used for growing quasicrystalline thin films

(2) Load Lock, for introducing samples into the system without bringing the whole system to ambient pressure

(3) An environmental gas cell, which is used to treat samples under controlled atmospheres with pressures ranging from 10^{-3} to 10^{-10} torr

(4) An analytical chamber, which houses various surface preparation and characterization tools which will be described shortly.

Standard 3mm TEM samples loaded in 5 mm Molybdenum rings can be easily transferred around the various side-chambers and also into the microscope via a detachable side-entry cartridge. The analytical chamber comprises a PHI 6050 duoplasmatron microbeam ion-gun for ion-beam cleaning the sample surface, a 1-10keV Kimball Physics electron gun(LaB_6) for electron beam annealing and a multi-purpose sample manipulation stage capable of 360° rotation, d.c. biasing, resistive heating and liquid N_2 cooling. The chamber also houses a Perkin-Elmer 04-548 dual anode x-ray tube (Mg and Al sources) with a PHI 10-360 spherical capacitance analyzer which can be used to acquire Auger electron spectrum(AES) or X-ray photoelectron spectrum(XPS) from surfaces. The AES is obtained using an FEI single lens schottky field-emission scanning electron gun. SEM images of the surfaces can be obtained using the same electron gun via a secondary electron

detector (Channeltron). In an innovative move, the scan signals from the SEM gun were used to drive the duoplasmatron scan coils, thereby adding the capability of imaging surfaces during ion-beam milling (Collazo-Davila et al., 1995).

2.2. TEM sample preparation

For all the material systems studied in this thesis, samples were made by conventional TEM sample preparation techniques. Highly pure oriented single crystals were obtained, either commercially or from collaborators, which were then cut into 3mm discs using an ultrasonic cutter. These were subsequently mechanically polished to a thickness of 100 microns and dimpled. After this, silicon samples were etched in an 90:10 HNO_3:HF bath to obtain a small hole at the center of the dimple. Attempts to make MgO samples employing an acid bath such as HNO_3 or $H3PO_4$ as an etching medium resulted in an extremely pitted surface which translates to poor mechnical stability of the sample. Hence this approach was discarded for all oxides; instead samples were made by ion-milling using 5 keV Ar^+ ions to perforation. The process of ion milling has two important effects on the sample:

(1) The near-surface region of the sample is non-stoichiometric, in particular oxygen deficient, due to the preferential sputtering of the lighter oxygen atoms compared to the cations

(2) The top few layers of the surface are amorphized and a wide array of bulk defects are created in the sub-surface region. Fig. 2.1 is a bright field image of an MgO sample obtained subsequent to ion-milling. One can

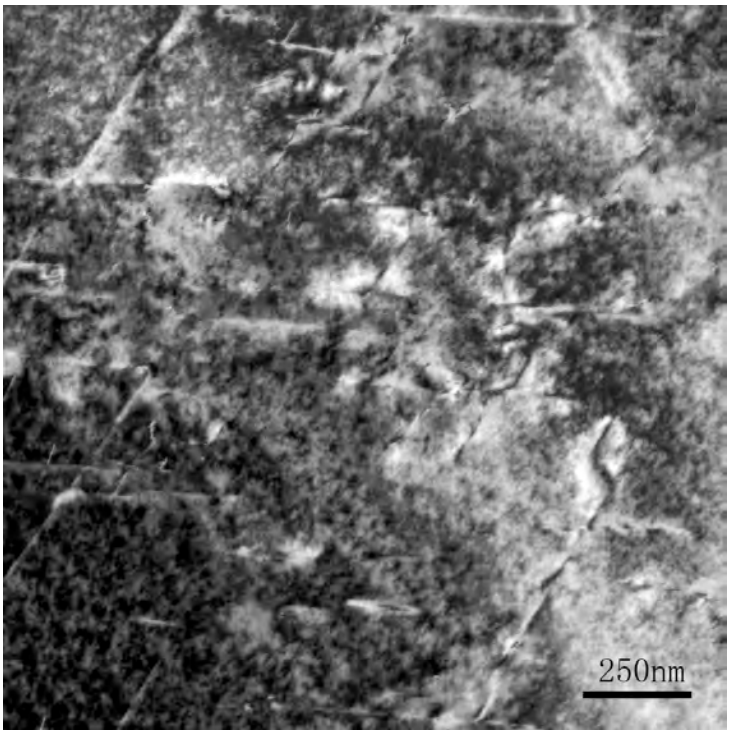

Figure 2.1. Bright field image of an ion-milled MgO sample

clearly discern the network of stacking faults and dislocations created by the ion beam.

Fortunately the damage inflicted by the sample preparation process can be reversed by annealing the samples at temperatures above $0.4T_m$ (melting temperature).

In the case of silicon, the native oxide must be removed and the subsequent annealing must be carried out *in situ* using an electron beam. However this approach when applied to MgO and $SrTiO_3$ samples yielded disastrous results with samples often disintegrating due to various electron stimulated desorption processes (Buckett, 1991). At the time of these experiments *ex situ* annealing in a tube furnace

approach was the only viable option for oxides (Presently, these anneals can be done *in situ* in the gas cell). Two different tube furnaces were employed to carry out the requisite anneals - a home-made furnace with a maximum operating temperature of 1100°C and a commercial Carbolite STF 15/51/180 furnace with a maximum operating temperature of 1500°C. TEM samples are placed in an alumina boat which is then placed inside a quartz tube sealed at both ends with fittings that provide for gas flow. The entire assembly is then inserted into the tube of the furnace and the temperature is ramped up/down at a controlled rate. High purity O_2 gas was flowed continuously thorughout the duration of the anneal; the effect of the atmosphere during annealing, in particular the partial pressure of O_2 is the subject of a current study (Chiaramonti and Marks, 2005). In this study, the only system that was found to be sensitive to the nature of gas flow was $SrTiO_3$ and the relevant details will be discussed in Chapter 5. The final annealing temperatures used for the various systems depending on the targeted surface structure and were arrived at using previously published work as a starting point.

At this juncture it is appropriate to discuss a few experimental tricks that have proved to be very useful: First is the effect of capillarity driven surface diffusion (Wong et al., 2000; Srolovitz and Safran, 1986). To briefly summarize the effect, a semi-infnite, uniform film on a substrate tends to contract from the edge to reduce the surface energy of the system and in this process, forms a thickened ridge followed by a valley. The valley sinks with time and eventually touches the substrate and the process starts over again, resulting in periodic mass shedding of the film.

This is a thermodynamic phenomenon and is applicable to all material systems. TEM specimens are analogous to thin films sans substrate and the aforementioned phenomenon has been widely observed and documented. This effect can be exploited to make ideal TEM samples since the valley that forms near the edge, if timed correctly, can be made extremely thin. Second is the the issue of surface versus bulk diffusion. Prolonged annealing at high temperatures where bulk diffusion is significant results in coarsening of the sample, rendering it unsuitable for further study. In the case of MgO and NiO, this temperature cutoff is around 1000°C, while the surface structures under scrutiny form at higher temperatures. One approach to circumvent this issue is to adopt a two or three step annealing process. By using a temperature profile shown in Fig. 2.2 , the time period over which the sample remains at high temperatures is minimized. The basic concept behind using these profiles is that the surface must be ordered before it can reconstruct and the temperatures required for ordering are much lower than those required for reconstruction. Another experimental tweak that worked well for silicon samples is to supply enough thermal energy initially to nucleate reconstructed domains on the surface and subsequently lower the temperature to allow for growth of these domains. In the case of systems where the reconstructions are temperature sensitive, this approach can be applied effectively only to the structure that forms at the lowest temperature.

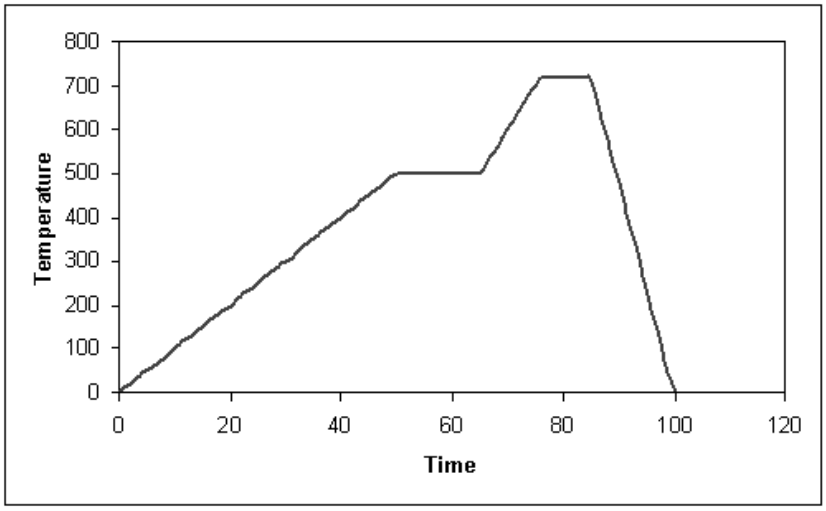

Figure 2.2. Two and three-step temperature ramping profiles used to minimize sample coarsening during high temperature anneals

2.3. Data acquistion and analysis

After annealing, the samples were introduced into the SPEAR system and studied using the UHV-H9000 microscope. The domain and step structures of surfaces are easily imaged using standard bright-field, dark-field and weak-beam imaging techniques. In addition to TEM experiments, *ex situ* AFM and SEM experiments were also performed on the same TEM samples, as necessary, to unequivocally characterize their surface morphology. These experiments, however, do not provide information about the atomic-scale structure of the surface. Despite the recent development of aberration corrected microscopes, diffraction is still superior to imaging when it comes to the study of surface structure.

Diffraction information from a small volume of material can be obtained by two different approaches : 1) Illuminate a large region of the sample and use a selected-area aperture (SA mode) to limit the region contributing to the diffraction pattern, or 2) Use a small probe (microdiffraction mode, use a smaller condenser aperture and spot size), thereby limiting the illuminated region. In the SA mode, regions outside the aperture may contribute to the diffraction pattern due to microscope imperfections (spherical aberration of objective lens) or user error (incorrect focussing of objective lens) (Hirsch et al., 1977). The effect is made worse by the fact that different sections of the diffraction pattern are from different regions of the sample. All the diffraction patterns used in this study were obtained by the second approach, namely microdiffraction. Typically the intensities of surface diffraction spots span over 2-4 orders of mangitude and hence a series of diffraction patterns with different exposure times were obtained form each surface. As with any experiment, one has to take care that the sample is not altered by the probing radiation and this is particularly important when dealing with a high energy electron beam. The effect of electron irradiation on oxides is a discipline that is well studied (Buckett, 1991). For most material systems, beam damage is a serious setback only when high fluxes are used, i.e. under conditions used in high resolution electron microscopy. In a diffraction experiment, where the fluxes are 2-3 orders of magnitude lower, it is not as big of an issue. Despite this, various precautions were taken to check for and minimize radiation damage. Instead of using monotonically increasing exposure times with constant auto-exposure setting,

the exposure times were intentionally offset with the long and short exposures uniformly spread out through the series. This helps in identifying any damage the structure might have suffered during the data acquisition process. In addition, a short exposure diffraction pattern was taken at the beginning and at the end of the exposure series to check for any decay in the structure. For long exposures, a particularly useful trick is to change the autoexposure setting so that the exposure time is shorter, keeping the net electron dose constant. For example, a 60 second exposure at an auto-setting of 60 seconds is equivalent in electron dose to a 2 second exposure with an auto-setting of 2 seconds. Using shorter exposure times minimizes the impact any uncontrollable external parameters (for example, instablilites in electronics, opening/closing doors, movement of people,..) may have on the experiment. Diffraction patterns were subsequently digitized to 8 bits with a 25 micron pixel size using an Optronics P-1000 microdensitometer. The microdensitometer was calibrated to be linear over the entire range of exposure series. Relative intensities of various surface diffracted beams were then measured using a cross-correlation technique developed and implemented using SEMPER image processing language in our group (Xu et al.). The measurements from multiple negatives were then reduced to yield one measurement and an associated error for every measured reflection following standard statistical methods (Collazo-Davila, 1999). These were then symmetry averaged to yield the final data set of symmetry independant beams.

2.4. Direct methods

Despite their ability to provide direct structural information at the atomic scale, imaging techniques are seldom sufficient to solve a surface structure due to limitations in the resolution from the weak signals. The resolution obtainable in a diffraction experiment is far superior and the process of data collection is parallel and fast, without the complications of radiation damage. Direct fourier inversion of these intensities is impossible since the phases of the scattered beams are lost in the diffraction experiment. However, the intensities can be used with various structure determining techniques, collectively known as direct methods, to yield a reasonable estimate of the true surface structure. Crystallographic direct methods have become popular for surfaces over the last decade and have been successfully used to solve various structures. In simple terms, direct methods exploit *a priori* information to constrain the phases of measured reflections. The common constraints used are:

(1) Atomicity : Scattering originates from atoms and hence the solution should have atomic features i.e. regions of large charge densities separated by charge-free regions.

(2) Positivity : Charge density in a real crystal is always positive

(3) Localisation : The region of space with significant atomic displacements (from bulk positions) is limited to the near-surface region.

The phases of the measured reflections cannot be totally random - i.e. they have to obey the above constraints and this can be used to gauge the 'figure of merit' (FOM) of a given set of phases. These constraints are iteratively imposed in a Gerchberg-Saxton fashion (Gerchberg and Saxton, 1972) using the projection onto convex sets algorithm (Combettes, 1996) to refine the phases of the measured reflections. The solution space is spanned effectively by a multi-solution search technique, namely the genetic algorithm (Goldberg, 1997; Landree et al., 1997). A detailed review of the theory behind direct methods for surfaces and the various details of the current implementation is published elsewhere (Marks, 1999; Marks et al., 2001b). The top solutions obtained from direct methods can be used to generate scattering potential (electron) or charge density (x-ray) maps. These maps with atoms assigned to regions of high intensity provide models that can then be used as the starting point for further refinements. Most often, only a part of the structure can be identified from these maps owing to unmeasured reflections and experimental errors. The various techniques employed for structure completion include fourier-difference methods, projection-based methods (Cowley, 1986) and heavy atom holography (Dorset, 1997). The structure so determined can be further refined by using the conventional R-factor or χ^2-type analysis against simulated data.

2.5. Studying charge density with electrons

The first sub-atomic particle to be discovered was the electron. Its discovery in the classic 1897 experiment of J. J. Thomson (in Cavendish Laboratory!) is arguably the single most important discovery of the last few centuries. The discovery spawned extensive research in a wide array of disciplines, all of which were aimed at understanding of the properties of electrons in condensed matter. When two atoms are brought together in close proximity the electrons in both atoms are redistributed such that the total energy of the combination is less than that of the sum of individual constituents. In this configuration, there is a net attractive force between the two atoms - a chemical bond. The theoretical and experimental tools necessary for a quantitative study of bonding in solids have been developed in the last quarter of the last century. Experimentally, both x-ray and electron scattering techniques can be used to study charge densities in solids. X-rays are scattered by the electrons in the solid while electrons are diffracted by the crystal potential, which is very sensitive to the charge density. The x-ray scattering amplitude of an isolated atom is called the x-ray atomic scattering factor (ASF, $f_x(s)$ in Eq. 2.1) and is defined as the fourier transform of the atomic electron density($\rho(r)$).

$$f_x(s) = \oint \rho(r) e^{2\pi i s r} dr \tag{2.1}$$

The ASF for x-rays ($f_x(s)$) and electrons ($f_e(s)$) are related by the famous Mott-Bethe formula:

$$f_e(s) = \frac{m_0 e^2}{2h^2 s^2} [Z - f_x(s)] \tag{2.2}$$

where, m_0 is the relativistically corrected electron mass, e is the electronic charge, h is the Planck's constant, Z is the atomic number and s is $\sin(\theta)/\lambda$. An important fact that is readily seen from Eq. 2.1 is that electron diffraction is very sensitive to changes in valence charge distribution at small scattering angles (i.e small values of s). These ASF's are available in parameterized form (as a sum of gaussians in the form $\sum_i a_i e^{-b_i s^2}$) in literature for almost all atoms and ions (Doyle and Turner, 1968; Rez et al., 1994). The densities used in these calculations, however, are obtained from first principles calculations of isolated atoms/ions and hence do not represent the density in a solid accurately. Also this type of parameterization doesn't lend itself to continuous refinement of the density while fitting experimental diffraction data. Alternatively, the atomic wavefunctions for various orbitals of atoms/ions are also published (Su and Coppens, 1998) and these can be used to fit the charge density of a solid. The idea is to use these wavefunctions as a basis set for describing the electron density in a solid and refining parameters that describe the density to fit the experimental data (Zuo et al., 1988). Various scattering models have been developed to this end:

(1) Spherical atom kappa formalism - In this model the atomic density is formulated as:

$$\rho_{atom} = \rho_{core} + \rho^{'}_{valence} = \rho_{core} + P_v \kappa^3 \rho_{valence}(\kappa r) \tag{2.3}$$

This model accounts for charge transfer (P_v) and the consequent expansion/contraction (κ) of the valence shell but does not consider aspherical distortions of density. This model when applied to x-ray data has proven to be quite successful and was found to give net charges which were in good agreement with accepted electronegativity concepts, and molecular dipole moments close to those from other experimental and theoretical methods (Brown and Spackman, 1991; Coppens et al., 1979).

(2) Multipole formalism - This model adds to the kappa formalism by including aspherical terms in the form of *atom centered multipolar functions*. The general formultion of the density in this case is:

$$\rho_{atom} = \rho_{core} + P_v \kappa^3 \rho_{valence}(\kappa r) + \sum_{l=0}^{l_{max}} \kappa^{'3} R_l(\kappa^{'} r) \sum_{m=0}^{l} P_{lm\pm} d_{lm\pm}(\theta, \phi) \tag{2.4}$$

where, R_l represents the radial part of the multipolar functions (usually chosen to be a nodeless density function based on hydrogenic orbitals), $d_{lm\pm}(\theta, \phi)$ are normalized real spherical harmonics that account for the aspherical component and $P_{lm\pm}$ are the population parameters for different multipoles.

The aforementioned models are both atom-centered models, and do not explicitly account for two-center density (i.e. density at the center of the bond axis). This shortcoming is easily overcome by adding a Gaussian term located between bonded atoms to describe bonding charge density (*non-atom centered deformation model*)(Brill, 1960). All these models have been used extensively to study the bonding in various molecules and solids (Zuo et al., 1997a; Coppens, 1997). To my knowledge, there haven't been any experimental studies that directly measure the charge density of a surface to date. In the present study, the kappa formalism was used along with non-atom centered gaussians to approximate bonding densities. Surface diffraction data from TEM is two-dimensional, i.e we measure the projected electron density of the surface. The multipole model, though more accurate in three dimensions, can be easily reproduced by using the kappa formalism in two-dimensions and non-atom centered bonding features can be used to account for any asymmetries.

CHAPTER 3

Reconstructions on MgO(111) Surface

3.1. Introduction

Magnesium oxide is thermodynamically very stable, has low dielectric constant and refractive index, and has been widely used as a substrate for growing various thin film materials. The oxygen lattice of MgO crystal matches well with those of perovskite oxide crystals as well as those of Si and GaAs crystals. MgO buffer layers were employed to grow high T_c superconductors (Wang et al., 1993; Tseng et al., 1994) and ferroelectrics (Hsu and Raj, 1992; Fork and Anderson, 1993) as well as nitrides (Tonouchi et al., 1987). Superconducting $YBa_2Cu_3O_{7-x}$ films were deposited epitaxially on MgO/GaAs (100) where MgO thin films were prepared by laser deposition or electron beam evaporation (Fork et al., 1992; Chang et al., 1992; Prusseit et al., 1992). Also, ferroelectric $LiNbO_3$ films were epitaxially grown on MgO (111) (Matsunaga et al., 1990), due to the excellent match of the MgO (111) atomic spacings with those in the a-b planes of $LiNbO_3$. Metal-ceramic oxide interfaces have also attracted a lot of attention over the last decade due to their extensive use in the myriad disciplines such as gas sensing, heterogenous catalysis and composites (Binns, 2001; Ertl and Freund, 1999; Teresa et al., 1999; Chambers, 2000). Metal adsorption on polar surfaces provides a mechanism to counter

the divergent electrostatic energy and stablize the surface. However, until recently, most of these studies were limited to precipitate-matrix interfaces in internally oxidized systems (Shashkov and Seidman, 1995; Chan et al., 1995). High-resolution electron microscopy and field-ion microscopy studies of the MgO/Cu {222} interfaces demonstrated that MgO precipitates are octahedrally shaped, with a cube-on-cube epitaxial orientation relationship with the Cu matrix. The interface was determined to be sharp, chemically and structurally and the precipitate was found to facet on {222}-type planes. The complete absence of non-polar (100) interfaces and the preponderance of anion terminated polar (111) planes in the interface was subsequently investigated through *ab initio* methods (Benedek et al., 1996). The polar interfaces were found to be significantly different from the non-polar ones, notably exhibiting larger works of adhesion and charge transfers/ stronger hybridization and electron-density oscillations extending into the metal. Theoretical studies on various other metal/MgO (111) polar interfaces reveal that the polar instability induces considerable electron transfer across the interface (resulting in polarization of the deposited metal) and an enhancement of the adhesion energy. Adsorption over an anion (O^{2-}) terminated (111) surface is energetically more favourable for most metals, except in the case of four metals: Pd, Ir, Pt and Au. Experimental studies of metal deposition on the extended polar MgO (111) surface found a transition from ionic to metallic adsorption of the metal species at a critical coverage of 0.15 ML (Magkoev et al., 2002). More recently, the polar MgO (111)-Fe_3O_4 (111) oxide-oxide interface was investigated using *in situ* XPS

and *ex situ* TEM (Lazarov et al., 2003). The polar interface was found to be stabilized by the formation of metallic Fe (110) nanocrystals and Fe_3O_4 (100) inclusions at the interface.

All the aforementioned studies do not account for any reconstruction of the oxide surface and assume the surface to be bulk terminated. It is evident that the surface polarity plays an important role in determining growth modes and interface structure and a polarity-compensated, reconstructed surface will behave differently under the same experimental conditions. Early LEED and SEM studies of the MgO (111) surface suggested faceting of the surface into three-sided pyramids of neutral (100) planes (Henrich, 1976). In this study, the samples were made by mechanical polishing, followed by hot phosphoric acid etch, brief ion milling and a final anneal in UHV at 1100°C. Similar results were reported for the same surface Onishi et al. (1987) and were consistent with the theoretical predictions based on relative energies of (100) and (111) surfaces (Tasker, 1979). Contradicting results were obtained from RHEED experiments on (100) and (111) surfaces of MgO (Crozier et al., 1992; Gajdardziska-Josifovska et al., 1991). Atomically flat, reconstructed (111) surfaces were obtained by using various sample preparation techniques including cleaving and mechanical/chemical polishing followed by annealing in O_2. This study also found that the impurity segregation to the surface upon high temperature annealing was suppressed for the (111) surface while it was inevitable on (100) surfaces. The apparent contradiction in literature was unequivocally resolved recently by Plass et al. (1998b).

Using optical, atomic force, scanning and transmission electron microscopies, the triangular pyramidal pits observed in prior studies were shown to be artifacts of the etching process. The surfaces of the pyramidal pits were vicinal {111}-type planes. The first surface reconstruction experimentally identified on the MgO (111) surface is the ($\sqrt{3}$x$\sqrt{3}$R30°) (Gajdardziska-Josifovska et al., 1991). Since then a variety of reconstructions have been identified on this surface including a (2x2) and ($2\sqrt{3}$x$2\sqrt{3}$R30°) (Plass et al., 1998a; Finocchi et al., 2004). The atomic structures of these surfaces are not established and have been the subject of recent studies.

In this chapter, the results from TEM studies of the ($\sqrt{3}$x$\sqrt{3}$R30°) and (2x2) MgO (111) surface structures are presented. First principles density functional (DF) calculations described in this chapter were carried out by Dr. O. Warschkow (VASP, pseudopotential) and Prof. P. Blaha (WIEN, full potential). The experimentally measured surface charge density is compared to those obtained from DFT calculations.

3.2. Sample Preparation and Surface Morphology

TEM samples of single crystal MgO ($\geq$ 99.95 % pure and Ca $\leq$ 40 ppm) were made from 3 mm discs that were dimpled, polished and ion beam thinned with 5 keV Ar^+ beam to electron transparency. These were subsequently annealed in a tube furnace under a flowing oxygen atmosphere to anneal out ion-beam damage and to order the surface. The surface reconstruction obtained was found to be a function of the annealing temperature used and to be independant of O_2 partial

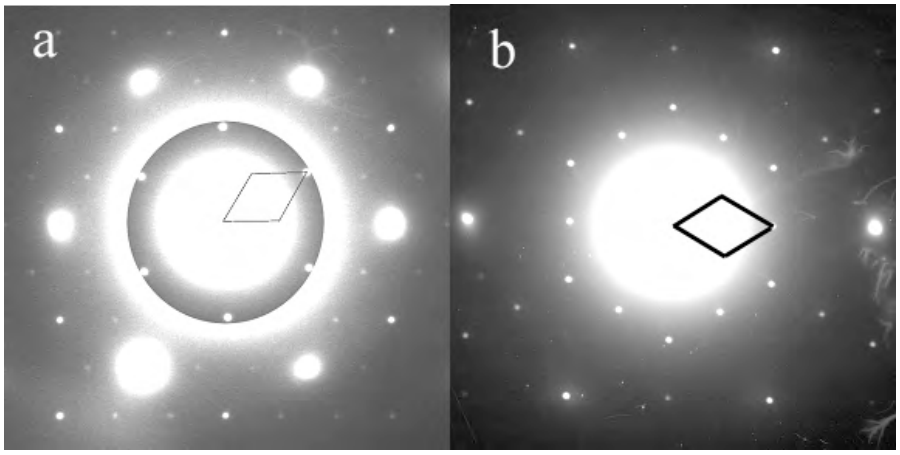

Figure 3.1. Diffraction patterns from (a)$\sqrt{3}$x$\sqrt{3}$R30° and (b) (2x2) reconstructions on MgO(111) surface. The surface unit cell is outlined in the figure.

pressure. However, it should be noted that all anneals were carried out in ambient air or under flowing O_2 and that no anneals were done in vacuum.

Figs. 3.1a & 3.1b show the diffraction patterns from ($\sqrt{3}$x$\sqrt{3}$R30°) and (2x2) reconstructed surfaces. The former was obtained by annealing the sample at 950°C and the latter at 1150°C. Fig. 3.2 is a dark field image obtained from the lower temperature anneal and is representative of both surfaces. The surface exhibits extended faceting with step bunches and the reconstructed terraces. The steps are winding, i.e. the kink density is relatively high, and the terraces are quite large, almost 200 nm wide. Notably, there are no voids in the subsurface region (from absence of speckled contrast), which were widely observed in other oxide systems (Erdman and Marks, 2003; Wang and Marks). Conventional AFM experiments were carried out with the same sample and Fig. 3.3 is an image (and line scan)

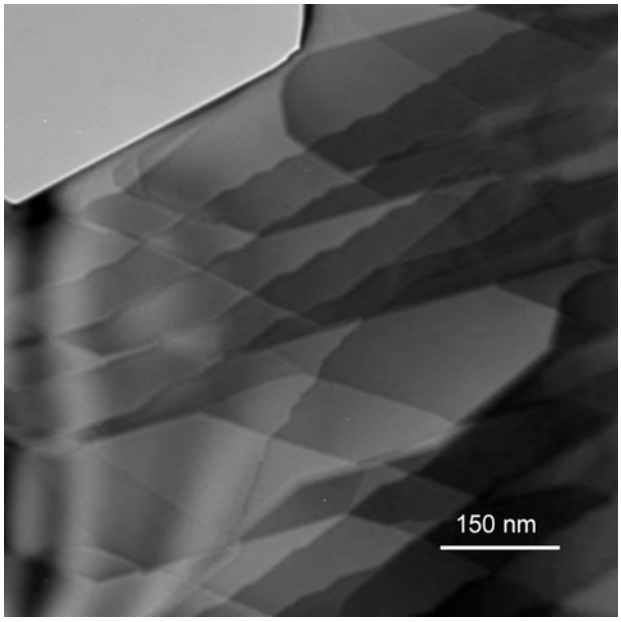

Figure 3.2. Dark field image from MgO (111)-$\sqrt{3}$x$\sqrt{3}$R30° surface. The morphology of the (2x2) surface is similar

obtained from the electron transparent regions of the sample. This experiment corroborates the TEM findings on surface morphology and also offers possibilities of measuring height differences between terraces for more quantitative studies of surface stresses.

3.3. MgO(111)-$\sqrt{3}$x$\sqrt{3}$R30° surface

The MgO(111)-$\sqrt{3}$x$\sqrt{3}$R30° reconstruction was the first observed by Gajdardziska-Josifovska et al. (1991) and was studied using RHEED and REELS. The surface was found to be remarkably stable in air, with the structure remaining intact even after a two month exposure to air. Surface sensitive REELS studies revealed that dominant surface species was oxygen. The only other study of this surface was

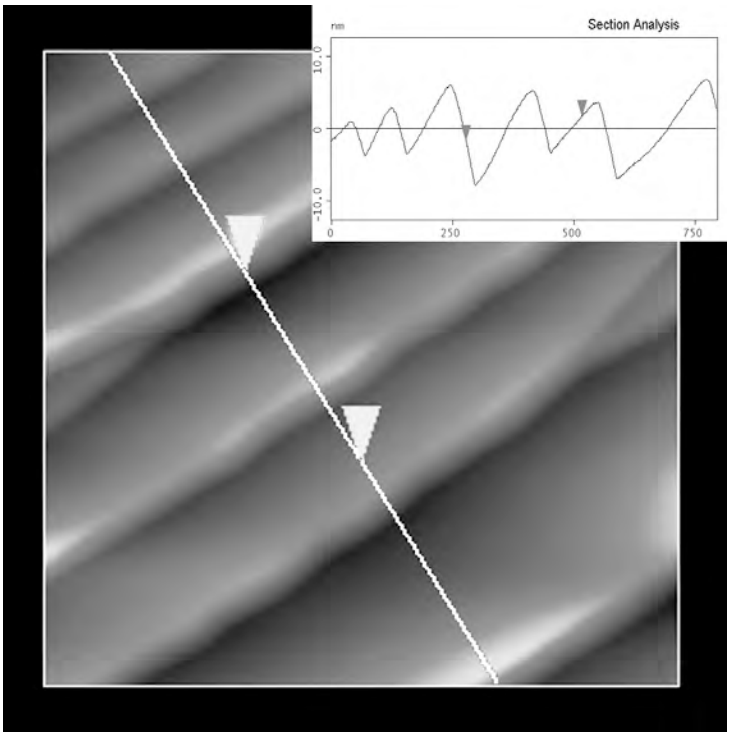

Figure 3.3. AFM image of a 650x650 nm^2 area of MgO (111)-$\sqrt{3}$x$\sqrt{3}$R30° surface (with inset line scan).

done by Plass et al. (1998a) who obtained the same reconstruction by annealing the sample in UHV at much higher temperatures (≥1450°C). From direct methods analysis of diffraction data, they proposed a surface structure terminated with oxygen trimers. Since this study was carried out under different annealing conditions, it cannot be directly compared to the present work.

Off zone-axis electron diffraction patterns, necessary for surface diffraction data analysis were obtained using the Hitachi UHV-H9000 electron microscope operated at 300kV at Northwestern University. TED patterns with varying exposure times were recorded from the surface using the techniques detailed in Chapter 2. Electron

Energy Loss Spectroscopic measurements indicated that the thickness was about 25 nm. The exposure series comprising ten negatives was subsequently digitized to 8 bits using an optronics negative scanner. Care was taken to ensure that under the exposure conditions the microdensitometer was linear. The intensities of 266 surface reflections were measured using a cross-correlation technique.

Direct Methods were used to solve the structure in *p3*, *p31m* and *p3m1* plane group symmetries. All three plane groups yielded similar solutions and the scattering potential map corresponding to the best solution is shown in Fig. 3.4a. This map with atoms assigned to the regions of sharp potential peaks (Fig. 3.4b)was used as starting point for the charge density refinements discussed later.

The structure that we determined, shown in Fig. 3.4b, is magnesium terminated with two Mg vacancies in the first layer. The surface is non-stoichiometric, in particular oxygen rich, consistent with previous Reflection Electron Energy Loss Spectroscopic studies (Gajdardziska-Josifovska et al., 1991). The oxygen atoms in the second layer and the Mg atoms in the third layer have small displacements from their bulk positions. The structure can be thought of as being comprised of complete $(MgO)_4$ octopolar units with two additional atoms in the fourth layer.

Theoretical studies on surfaces of ionic rock-salt oxides predict that they should be terminated with complete $(MgO)_4$ units (Wolf, 1992). The octopolar units ensure charge neutrality of the surface and also have rapidly decaying electrostatic interactions. However, such octopolar models assume that the surfaces reconstruct stoichiometrically; the validity of this model in the presence of excess oxygen or

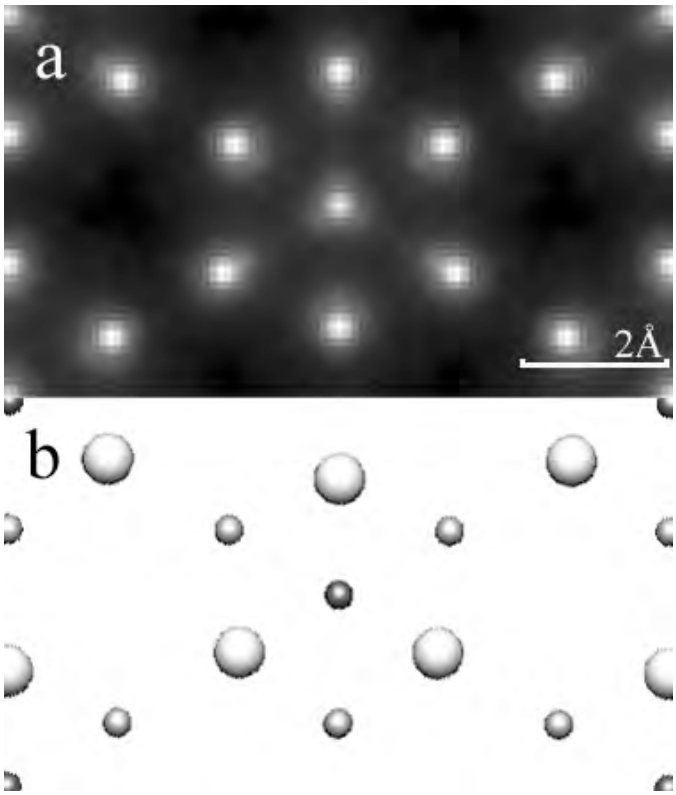

Figure 3.4. (a) Direct Method map for MgO(111)-$\sqrt{3}$x$\sqrt{3}$R30° surface (b) Top view schematic diagram of the same surface. Large circles correspond to O atoms and the smaller ones are Mg atoms

magnesium is not clear. Also, this result is valid only if both the anion and the cation retain their bulk oxidation states. This is seldom the case since the atoms in the near surface region are co-ordinated differently from the bulk.

3.3.1. Fitting the Bulk Charge Density

To better understand the stabilizing forces behind this surface reconstruction, we attempted to fit the surface charge density in addition to atomic positions of the

surface atoms. Following Dawson (1969) and Stewart (1973), the atomic scattering factors were parameterized as:

$$f_{Mg}(s) = \sum_{1s,2s,2p} f_{Mg,n}\left(s/\kappa_n\right) + q_1 f_{Mg,3s}\left(s/\kappa_{3s}\right) \tag{3.1}$$

$$f_O(s) = f_{O,1s}\left(s\right) + q_2 f_{O,2s}\left(s/\kappa_{2s}\right) + 3q_2 f_{O,2p}\left(s/\kappa_{2p}\right) \tag{3.2}$$

where $f_{A,n}$ is the scattering factor of orbital n for species A, κ_n is the expansion/contraction parameter of the orbital, q_1 and q_2 the occupancies of Mg 3s and O 2s orbitals respectively. These were converted to electron scattering factors subsequently using the Mott formula. We would like to note that such parameterizations are intrinsically non-convex: such charges and bondorders are, by their nature, highly basis-set dependent. Owing to this, the charges reported in this work should not be understood in absolute terms; it is the trends (increase or decrease versus a reference) in these charges that is meaningful.

We first fitted to the published bulk structure factors of MgO to determine a reference point. The deeply bound 1s core orbitals of both atoms are not significantly affected by crystal fields and hence their relaxation parameter was fixed at unity. The wavefunctions for the various orbitals in Eq. 3.1 & 3.2 were obtained from the self-consistent field calculations of (Su and Coppens, 1998). Gaussian

bonding terms of variable width (B_n) and magnitude (q_n) located between adjacent Mg-O atoms and O-O atoms were also used in some fits. The scattering from these "bonds" has the form $q_n e^{-B_n s^2}$ in Fourier space. Table. 3.1 lists the various fits to the published bulk structure factor measurements of MgO by Zuo et al. (1997b), Lawrence (1973) and Sanger (1969). In addition to the aforementioned data sets, a mean inner potential of 12.52(24) V (Kim et al., 1998) was also used in the fitting process. Isotropic Debye-Waller factors for Mg and O atoms included in the refinements were fairly constant and are estimated at $B_O = 0.335 \mathring{A}^2$ and $B_{Mg} = 0.308 \mathring{A}^2$, which is in excellent agreement with previous studies (Zuo et al., 1997b; Lawrence, 1973).

Starting from the wavefunctions of Mg and O^-, various fits were attempted using a slightly modified version of the NL2SOL code from the port3 library. Table 3.1 is a partial list of the various fits attempted and it is evident that the bulk charge density is well approximated by superposition of spherically symmetric atomic densities. The non-spherical components treated by the bond densities between cation-anion and anion-anion pairs are very small. The atomic scattering factors of Mg (in MgO) obtained from fit four are almost identical ($\leq$1%) to those of Gillet and Cortona (1999), while the omission of the charge in Mg-O and O-O bonds results in small differences ($\leq$2%) for O at low angles. It is well established that the oxidation state of Mg in bulk MgO is close to +2 and hence the fit that can be interpreted most physically is fit four (Zuo et al., 1997b). For all subsequent

refinements of surface structure, the parameters of surface atoms were initialized from this fit.

3.3.2. Fitting Surface Charge Density

The in-plane positions of the second layer O and third layer Mg atoms, the relaxations and occupancies of the atoms in the top two layers were allowed to vary. The Mg atom in the third layer was constrained to be identical to the bulk Mg atom. In all refinements, the relaxations of the 2s and 2p orbitals of O were coupled i.e. they were constrained to vary preserving the κ_{2s}/κ_{2p} ratio and the surface was constrained to be charge neutral. Table. 3.2 summarizes the results of the various fits to the surface data. In all cases the x,y positions refined to almost identical values which are shown in Table. 3.2, together with the z-positions from density functional calculations discussed later. The z positions were not used in the density fitting process since TED is sensitive only to projected potential. Experimental data were fitted with various combinations of variables. In the first fit, the relaxations of the 2s and 2p orbitals of Mg are coupled while they are independent in the second fit. The valence shell relaxations and occupancies of both species are almost identical even though the 2s and 2p orbitals have very different relaxation parameters. The same is observed in the third fit where the 2s and 2p orbitals of Mg were forced to keep their bulk values. The addition of a Mg-O bond term, similar to the one in bulk fitting, results in the siphoning of the electrons from the valence orbitals of Mg to those of O and the bond. If we simply

Table 3.1. Results of model fitting of bulk charge density of MgO. B_3 and q_3 are parameters for the Mg-O bond, while B_4 and q_4 correspond to the O-O bond (see text for details)

	Mg			O								
Fit No	$(\kappa_n - 1)\%$ 2s	$(\kappa_n - 1)\%$ 2p	$(\kappa_n - 1)\%$ 3s	$(\kappa_n - 1)\%$ 2s	$(\kappa_n - 1)\%$ 2p	q_1	q_2	q_3	B_3	q_4	B_4	χ^2
1	13.7	-5.2	25.0	-16.4	1.8	0.26	1.93					1.42
2	18.9	-6.8	9.6	-10.4	0.4	0.19	1.90	0.04	6.70			1.20
3	12.1	-4.7	24.9	-14.2	1.0	0.20	1.93			0.01	1.74	1.38
4	18.2	-6.7	-25.0	-7.7	-0.7	0.06	1.90	0.04	7.35	0.02	2.76	1.11

Table 3.2. Results of model fitting of charge density of MgO(111)-$\sqrt{3}$x$\sqrt{3}$R30° surface

Fit	Mg			O						
No	$(\kappa_n - 1)\%$ 2s	$(\kappa_n - 1)\%$ 2p	$(\kappa_n - 1)\%$ 3s	$(\kappa_n - 1)\%$ 2s	$(\kappa_n - 1)\%$ 2p	q_1	q_2	q_3	B_3	χ^2
1	3.9	-18.0	5.0	-8.3	-1.5	0.43	1.87			1.49
2	-10.6	-15.0	5.0	-8.6	-1.8	0.38	1.88			1.51
3	18.2	-6.7	5.0	-4.3	2.8	0.43	1.87			1.57
4	2.8	-18.8	-18.0	-10.7	-4.0	0.00	1.89	0.08	2.32	1.50

take the orbital occupancies as a measure of the oxidation states, we find for the top Mg and second layer O atoms +(1.65 ± 0.1)e and -(1.52 ± 0.1)e respectively, relative to bulk values of +1.94e and -1.72e (ignoring the charge located between the Mg and O atoms, q3 in Tables. 3.1 & 3.2). As noted before, the partitioning of charge density into a set of atomic orbital basis functions is a non-convex problem with multiple solutions. All the above fits represent the same density and represent the various minimas inherent in multi-variable optimization. In some respects these numbers are misleading, and a better physical interpretation is to look at the two-dimensional projected valence shell deformation density shown in Fig. 3.5. Although there is more nominal charge in the Mg 3s orbital, the valence orbitals are expanded with respect to the bulk atom which results in a negative difference in the region very close to the core. The O atom is contracted with respect to the bulk, consistent with less charge in its valence shell, which is reflected in the negative contours around the O sites. The electron hole in the second layer is quite diffuse, spread over a radius of ∼1Å centered on the O sites. An interesting feature that is evident in the deformation map is the region of increased density along the Mg-O direction indicative of a weak covalent bond, manifested as the truncation of the negative lobe around the O sites.

3.3.3. DFT calculations

3.3.3.1. Methods. The MgO surface structure was separately optimized using a DFT surface slab model. This provides for both an independent confirmation of the

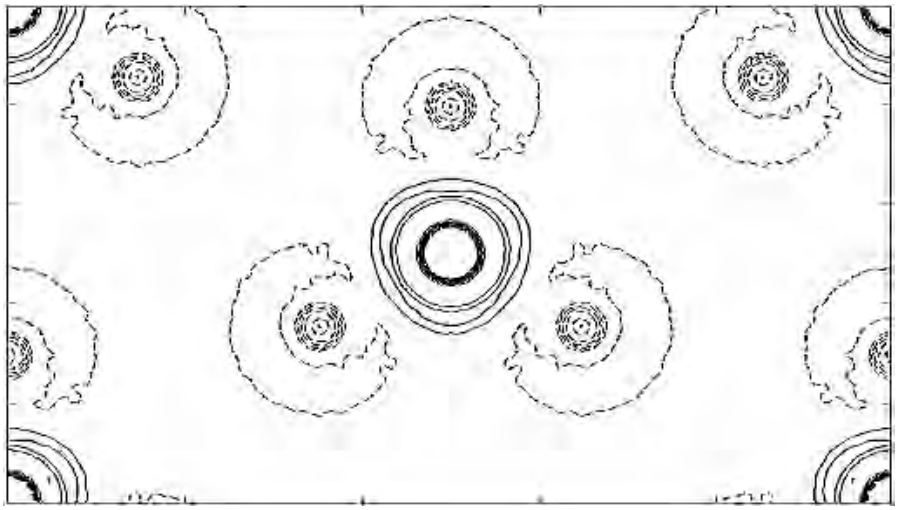

Figure 3.5. Deformation charge density map projected onto the (111) plane. The contour interval is 1.5 x 10^{-4} $e^{-}/\mathring{A}^2$

experimentally determined x,y (or in-plane) atomic positions as well as the missing z atomic positions. The slab model is 3-dimensionally periodic and contains 13 layers (35 atoms) of MgO separated by at least 14 $\mathring{A}$ of vacuum. The calculations were performed using the ab-initio total energy program VASP (Vienna ab-initio simulation package) (Kresse and Hafner, 1993, 1994a; Kresse and Furtmuller, 1996a,b) as well as the full-potential all-electron (linearized-)augmented-plane-wave + local orbitals (L/APW+lo) method as implemented in the WIEN2k code (Blaha et al., 2001). The relevant calculational details of the VASP calculations are as follows: The GGA approximation (Perdew, 1991; Perdew et al., 1992), Vanderbilt ultrasoft pseudopotentials (Vanderbilt, 1990; Kresse and Hafner, 1994b) and a plane-wave basis set with a 400 eV cut-off were used. Brillouin zone integrations were performed on a 4x4x1-Monkhorst-Pack grid (Monkhorst and Pack, 1976). In

Table 3.3. Experimental and theoretical (both, from VASP and WIEN2K calculations) Co-ordinates (x,y coordinates from WIEN2K are identical to VASP and not given explicitely) of the various atoms in MgO(111)-$\sqrt{3}$x$\sqrt{3}$R30° surface. $a = b = 5.15\mathring{A}$ $c = 7.30\mathring{A}$ $\alpha = 90°\beta = 90°\gamma = 120°$.

		Experiment		VASP			WIEN2K
Layer	Atom	x	y	x	y	z	z
1	Mg	0	0	0	0	0.627	0.627
2	O	0.294	0	0.321	0	0.499 0.498	
3	Mg	0.662	0	0.652	0	0.344	0.343
4	O	0	0	0	0	0.168	0.167
4	O	1/3	2/3	1/3	2/3	0.168	0.168
4	O	2/3	1/3 2/3	1/3	0.168	0.168	
5	Mg	1/3	0	0.332	0	0	0

the structure optimization, all internal coordinates were positionally relaxed; the unit cell dimensions were held frozen. For the WIEN2K calculations we used the PBE-GGA (Perdew et al., 1996), which is similar, but not identical to the VASP calculations. The atomic sphere radii were chosen to be 1.65 and 1.7 bohr for Mg and O, respectively. A well converged APW+lo basisset [APW+lo] described by $R_{MT} * Kmax = 6.5$ (this corresponds to a PW cut-off of 211 eV) with 226 additional local orbitals for Mg 2s,2p and O 2s orbitals was used and the charge density/potential was expanded up to L=10.

3.3.3.2. Structural refinement. The structure was modelled by a periodic slab model of 13 layers (35 atoms), separated by 14 $\mathring{A}$ of vacuum. The cell dimensions were kept fixed, but the internal positions of the atoms were refined with the help of

the calculated forces on the atoms. The results are listed in Table. 3.3. A comparison of the theoretical x and y positions with experiment reveals overall quite good agreement, although in experiment the oxygen atom has a stronger deviation from the ideal (undistorted) x-position than in theory. It is worth mentioning, that both theoretical methods give identical x,y coordinates (at least to the accuracy listed in Table. 3.3. As mentioned above, the z-coordinate cannot be measured by experiment, but has been determined theoretically. Again almost perfect agreement between the two theoretical methods has been found. The "bulk" layer seperation corresponds to z=0.166 and it is evident that the top O-layer (layer 2) is almost at the ideal height, while both adjecent Mg-layers are drastically contracted towards the O layer. Of course the effect on the "partially empty" top-Mg layer is even more pronounced.

3.3.3.3. Theoretical deformation plots. To obtain a theoretical deformation map that can be compared against the experimental results, full potential calculations were carried out employing WIEN2k DFT code (Blaha et al., 2001). Oxygen, which is of course in a highly ionic state (see later), is not stable as a free O^{2-} ion within DFT. However, one can simulate the stabilizing effect of the cations of the crystal by a Watson sphere model, i.e. by adding the potential of a positively charged sphere (Q=+2) with a "Watson radius" R_W. The resulting free ionic O^{2-} charge density depends of course on the chosen R_W. Figs. 3.6a-c show the deformation densities (the difference between the crystalline density and a superposition of free ionic Mg^{2+} and O^{2-} densities) on the (100) plane normal to the (111) surface.

The difference between the three plots is the radius of the Watson sphere used to stabilize the O^{2-} reference ion (Watson, 1958) leading to more (smaller R_W) or less contracted ionic O^{2-} densities. From the residual charge density around bulk atoms further down in the structure, it is evident that the density in MgO is close to an O^{2-} density stabilized by R_W ≈2.5 bohr (Fig. 3.6b. The smallest residual (w.r.t bulk Mg and O) was obtained for a R_W of 2.4 bohr. Figs. 3.7a & b show the corresponding deformation maps which are in excellent agreement with experimental observations, namely an increased density (less ionic) on the surface Mg atom and correspondingly a reduced density around the subsurface O atoms. The surface Mg atom shows a large dipolar anisotropy normal to the surface with negative deformation density (less charge in the crystal compared to the superposed ionic densities) towards the bulk. The second layer O atoms are also polarised considerably with more density along the Mg-O bond axis. Perturbations of charge density beyond this layer are minimal (which is consistent with the experiment).

3.3.3.4. Charge analysis. Charge transfer is an important quantity to characterize the nature of a chemical bond, but since atoms cannot be defined uniquely in a solid, the corresponding charge transfer will always be dependent on the underlying model. This is true for both theory and experiment, where the interpretation of the experimentally measured structure factors also depends a lot on the model used to fit experiment. In this section we compare the experimental charges obtained via a kappa model with the theoretical charges obtained via Bader's "atom

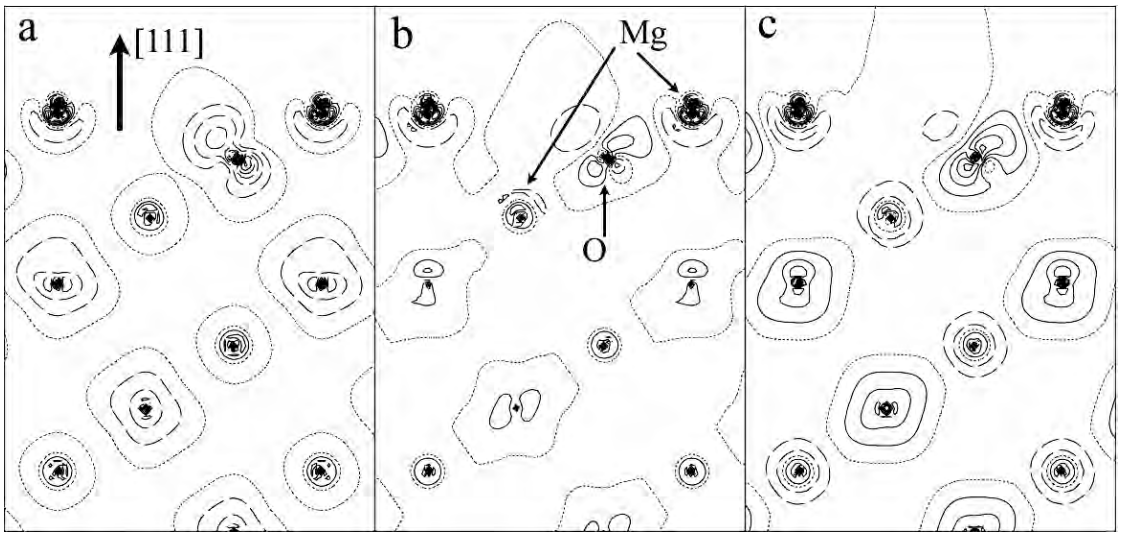

Figure 3.6. Deformation maps on (100) plane with different radii for O R_W (a) 2.0 bohr (b) 2.5 bohr and (c) 3.0 bohr. The contour interval is $0.05e/\mathring{A}^3$ and full, dotted and dashed lines indicate positive, zero and negative contours. (see text for more details)

Table 3.4. Charges (in e^-) inside Muffin-Tin atomic spheres (Q^{MT}) and within the atomic volume according to Bader's AIM theory (Q^{AIM}) as well as ionicities according to AIM-theory (q^{AIM}), an empirical bond-valence model (q^{bv}) and from the experimental multipolar model (q^{exp}).

Layer	atom	Q^{MT}	Q^{AIM}	q^{AIM}	q^{bv}	q^{exp}
1	Mg	10.101	10.35	+1.65	+1.69	+1.65
2	O	7.711	9.46	-1.46	-1.67	-1.52
3	Mg	10.082	10.29	+1.71	+2.00	+1.94
4	O	7.773	9.64	-1.64	-1.77	-1.96
4	O	7.809	9.68	-1.68	-1.94	-1.96
5	Mg	10.079	10.29	+1.71	+1.95	+1.94

in molecule" (AIM) theory (Bader, 1990) as well as with an empirical bond-valence model.

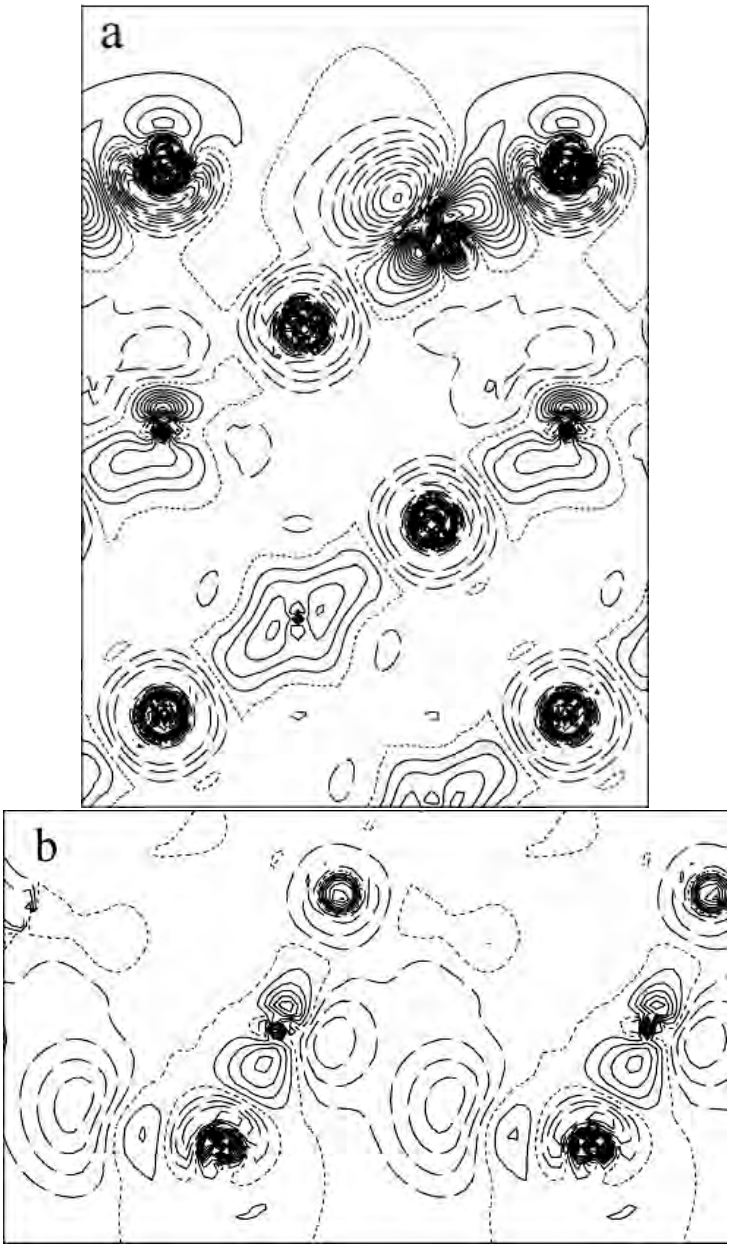

Figure 3.7. Deformation maps using O R_W of 2.4 bohr (a) (100) plane and (b) (111) plane. The contour interval is 0.02 $e/\mathring{A}^3$

The empirical bond-valence model, going back to Pauling, is based the observation that the distances an atom forms with its nearest neighbors is simply correlated with its charge state. Partial atomic charges can thus be derived in a straightforward manner requiring only the atomic positions (here the DFT optimized structure) and a set of "universal" parameters (Brese and O'Keeffe, 1991). The results are included in Table. 3.4, and for the top atoms they correlate very well with what was found in the experimental fits. The changes in bond lengths lower down in the structure also yield some apparent bond-valence changes. Tests where these were added to the experimental refinements indicated that these degraded the fit to the data, so these are presumably artifacts of the empirical method.

A widely used method to analyse both experimental and theoretical charge distributions is based on Bader's AIM method (Bader, 1990). In this method, space is partitioned into atoms by defining an atomic surface as a surface of zero flux, i.e. $\nabla\rho.\vec{n} = 0$. AIM analysis of the total charge density (from the all-electron WIEN2k calculations) was carried out to quantify the nature of the surface bonding in the $\sqrt{3}$ surface. The advantage of using the AIM partitioning scheme over Mulliken and Löwdin schemes (Mulliken, 1955; Löwdin, 1953) is that AIM charges are uniquely defined for a given density (independent of basis sets). Table. 3.4 lists the charge inside the atomic spheres (of R_{MT} = 1.65 and 1.7 bohr for Mg and O spheres, respectively) and the corresponding AIM charges as well as the resulting ionicities according to AIM, bond-valence and kappa (experimental) model. The Bader charge for the "bulk" atoms further down in the structure(atom 6 is representative

for all bulk atoms) is about ±1.71. The surface O (atom 2) has much less charge (the "electron hole") and this reduced charge is also visible (to a smaller extent) inside the spheres. On the other hand, the surface Mg is less ionic in the AIM charges and we also find an increased charge density inside the sphere (i.e. less charge transfer from this surface Mg to the O atoms). It is also evident that only the surface Mg is affected, while for O this compensation is more long ranged (only O in layer 6 comes close to the bulk value of -1.71). Although the changes in AIM charges of surface atoms relative to bulk are in good agreement with the experiment, the magnitudes of the relative changes are different. This can be simply explained by the following argument: The charges inside MT spheres for bulk Mg atoms (atom 6) point to a contracted Mg atom in the bulk lattice (seen in the fitting of the bulk structure factors). In experimental fits, the charge in the interstitial region was fitted using an expanded O atom (thus giving partial charges of ±1.96 for bulk) while Bader partioning results in a different reference state (±1.71).

3.3.3.5. Topological analysis. Bader's AIM theory does not only give a definition of an atom in a molecule, but in addition it tries to characterize chemical bonding by the topology of the charge density. For this purpose one searches for so called critical points (CP). The most important ones are bond critical points, which correspond to saddlepoints in the density and are typically found between neighboring atoms (which form a "bond"). Besides its position (distance to the

Table 3.5. Selected (3,-1) bond critical points of bulk MgO and MgO(111)-$\sqrt{3}$x$\sqrt{3}$R30° surface charge densities

adjacent atoms	$\rho(e^-/\mathring{A}^3)$	$\Delta\rho(e^-/\mathring{A}^5)$	dist-atom1($\mathring{A}$)	dist-atom2($\mathring{A}$)
Mg(1) - O(2)	0.430	10.34	0.83	1.07
Mg(3) - O(2)	0.287	6.93	0.89	1.16
Mg(3) - O(2)	0.286	6.61	0.89	1.18
Mg(5) - O(4)	0.267	6.04	0.90	1.19
Mg(3) - O(4)	0.204	3.16	0.94	1.27
bulk Mg - O	0.262	3.75	0.89	1.22
O(2) - O(4)	0.123	1.07	1.47	1.46
Mg(5) - Mg(5)	0.121	0.97	1.48	1.48
O(6) - O(6)	0.119	0.98	1.49	1.49
bulk O - O	0.119	0.94	1.49	1.49

adjecent atoms) and the density at this point, the Lapalcian is also used to characterize the bond as more or less closed-shell interactions. Table. 3.5 lists the most important bond critical points (BCP's) of the MgO(111) surface charge density and compares them with bulk MgO. From this table it is evident that the bonding near the surface is quite different from that in the bulk. One finds clearly defined BCP of type (3,-1), with a much larger density (0.43 $e^-/\mathring{A}^3$) between the surface Mg and the subsurface O atom than between other Mg-O neighbors or in comparison to bulk MgO (typically 0.26 $e^-/\mathring{A}^3$). The Laplacian is positive and even larger than in bulk MgO CP, typical of closed-shell interactions with reduced bond distance. Besides many other CPs in this complicated structure we list a few BCPs characterizing the next-nearest neighbor bonding (O-O contact in buk MgO). In

all cases the density is rather constant and very close to the bulk value, indicating that the densities remain rather constant in this positions.

3.3.3.6. DOS. Figs. 3.8 & 3.9 show the density of states(DOS) of the various surface atoms. It is clear that the band gap is reduced from 5 eV for bulk to 2.5 eV for the surface. This change is primarily brought about by the s and p_z states of the top Mg atom at the bottom of the conduction band. The Fermi surface is just under the edge of the valence band and hence the surface is technically metallic, however these states could be easily filled by extra electrons from an extended bulk. Similar trends are seen in the valence band of second layer O atom with the unfilled states in the band coming from p_x and p_y orbitals.

The $\sqrt{3}$ reconstruction of the MgO (111) reconstruction is Mg-deficient, lacking half an Mg per $\sqrt{3}$ surface unit from stoichiometry. If one formally considers the surface composed of Mg^{2+} and O^{2-} building blocks, an additional electron hole per surface unit is required to make the reconstruction charge neutral. Thus, in the electronic structure of the surface we expect two types of phenomena:

(1) Local increases (more positive and less negative, for cations and anions, respectively) of partial atomic charges with respect to bulk due to the presence of the electron hole at these sites.

(2) Changes in covalency caused by the truncation of coordination polyhedra of near surface atoms. An increase of covalency would be evinced by both

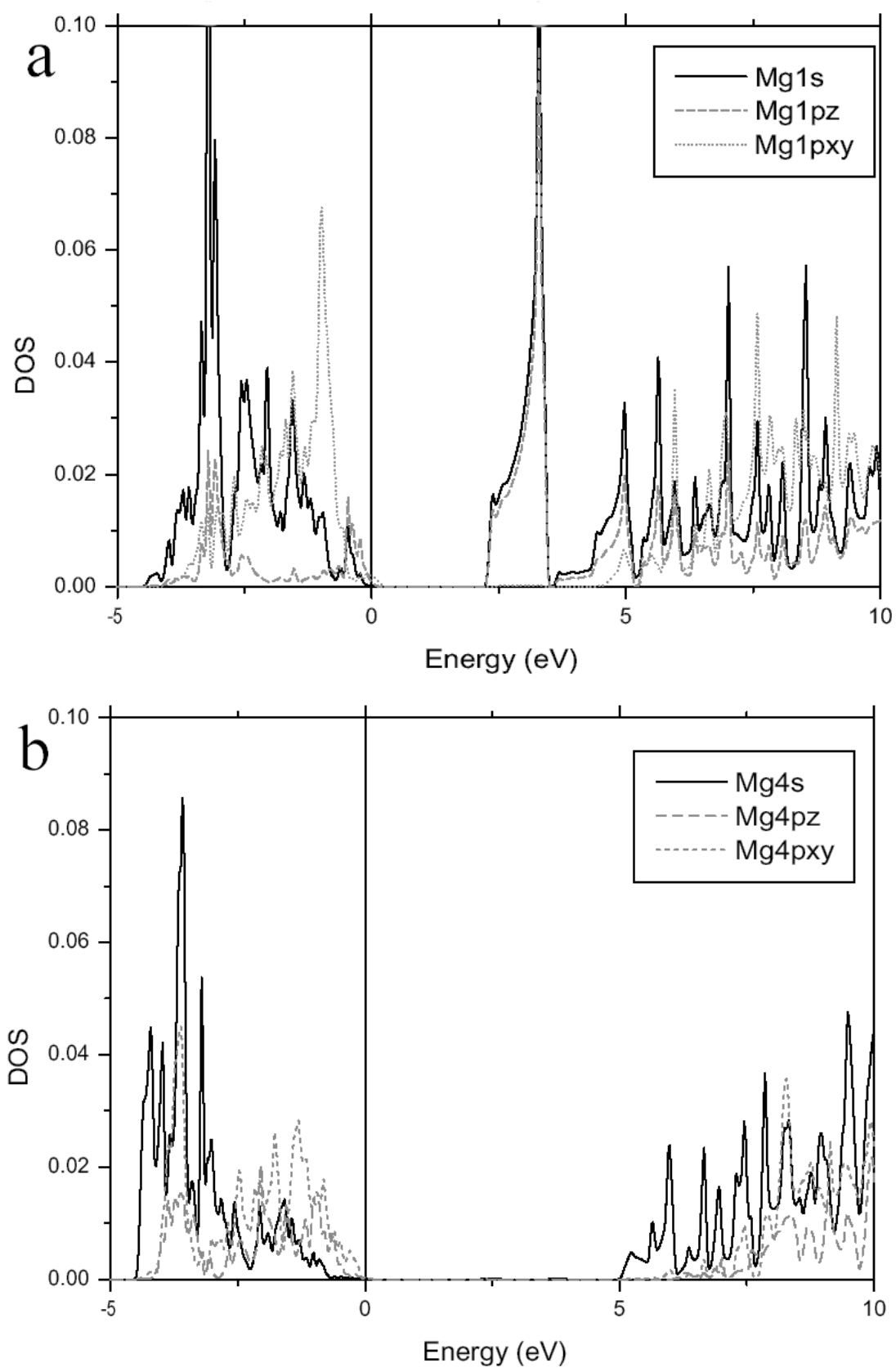

Figure 3.8. DOS plot for (a) surface(top layer) and (b) bulk Mg atoms

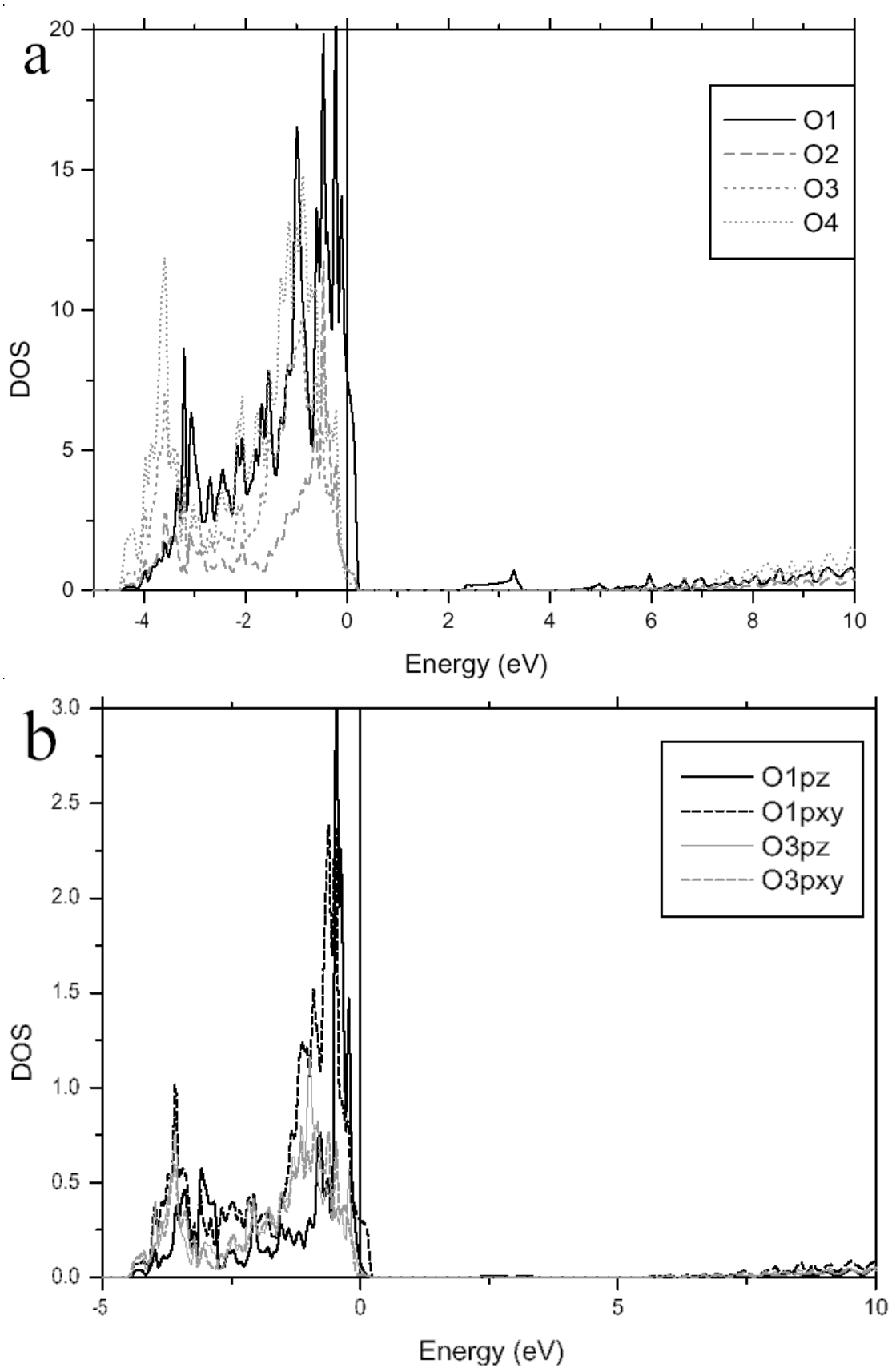

Figure 3.9. DOS for (a) surface and (b) bulk O atoms

an absolute decrease (cations and anions become less positive and less negative, respectively) in the partial atomic charges, and, more significantly, in an increase in the calculated bond-populations.

The reduction in charge due to a near-surface covalency increase is more than counterbalanced by the fact that there is more positive charge in the vicinity of the surface due to presence of an extra electron hole. Intuitively, this is perhaps surprising since a covalency increase, that is, a build-up of electron density in between 1st and 2nd layer atoms, takes place in environment in which there are fewer electrons around.

3.4. MgO(111)-2x2 surface

Theoretical studies have long demonstrated that the surface of ionic rocksalt oxides should be reconstructed at zero temperature. This conjecture was introducted to avoid the classic *Madelung problem* of ionic materials, namely the divergence associated with the r^{-1} term in the coulomb potential of condensed systems. It was demonstrated that the effective coulomb potential in a perfect ionic crystal at zero temperature decreases as r^{-5} (Marathe et al., 1983). This result was obtained by viewing the MgO lattice as a simple cubic Bravais lattice with a $(MgO)_4$ basis. Using an octopolar basis which has no net dipole or quadrupole moments avoids the generation of long-range polarization, making it easier to evaluate the Madelung energy. The result generalized by Wolf (1992) by using a dipolar MgO basis, without

assigning fractional ionic charges to the summation unit or assuming that the basis molecule has vanishing lower order electrostatic moments. With this approach the octopolar reconstruction was proposed as a mechanism to minimize surface-dipoles without requiring point defects. To date only two experimental studies of MgO (111)-2x2 surface have been published. In the first study, the surface was prepared by annealing in a vacuum furnace ($5x10^{-7}$torr), and the proposed surface structure had oxygen trimers (Plass et al., 1998a). The second study was carried out using synchrotron surface x-ray diffraction and the surface was prepared by an initial anneal in air followed by anneals in vacuum under different partial pressures of O_2 (Finocchi et al., 2004). Fig. 3.10 shows the variations observed in the relative intensities of (1,1) and (1,0) surface diffraction spots with changes in temperature and O_2 partial pressure. This was interpreted due the co-existence of two different reconstructions (low temperature or LT and high temperature or HT), both with the (2x2) unit cell, but with different atomic structures. An oxygen terminated octopolar structure was proposed for the LT phase and an (0001)-oriented epitaxial Mg layer on O-terminated MgO(111) (hereafter, just epi-Mg) was proposed for the HT phase.

In the present study, TEM samples of single crystal MgO(111) were made by techniques discussed in Chapter 2 and the (2x2) reconstruction was obtained by annealing under a flowing O_2 atmosphere at 1150°C. Diffraction data from the (2x2) surface was collected and analyzed using the same methodology employed for the $\sqrt{3}$ reconstruction. The scattering potential map obtained from Direct

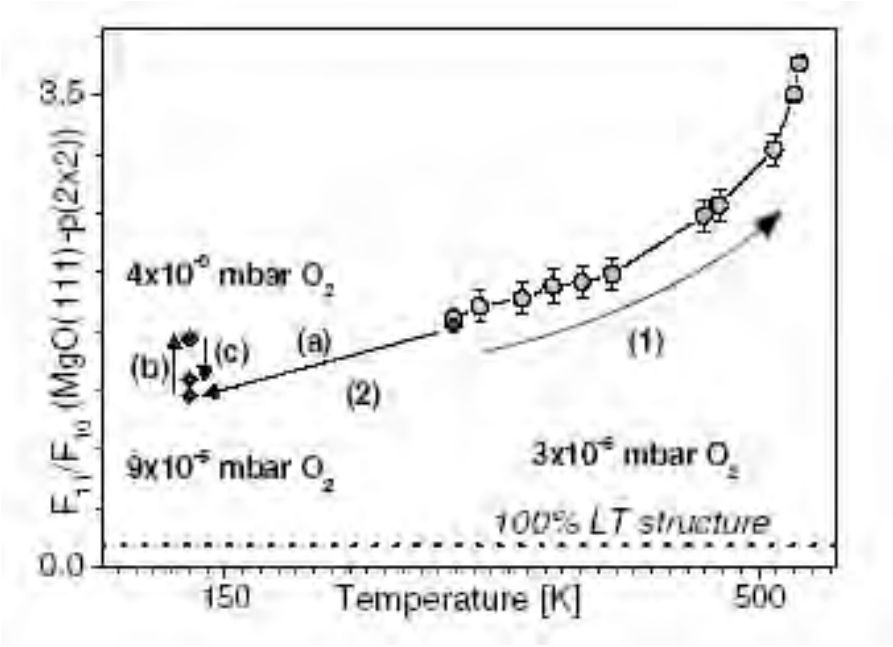

Figure 3.10. Ratio of the in-plane intensities of (1,1) and (1,0) reflections of the MgO (111)-2x2 surface as a function of temperature and oxygen partial pressure. (1) T increases and $p_{O_2} = 3x10^{-5}$ mbar (2a) T decreases and $p_{O_2} = 9x10^{-5}$ mbar. At low temperature, p_{O_2} is first decreased (2b) to $4x10^{-6}$ mbar and then increased again (2c) to $9x10^{-5}$ mbar. The horizontal dotted line indicates the expected ratio for the LT pure structure, while a ratio of 11.6 corresponds to the HT structure. see text for more detials. (Finocchi et al., 2004)

Methods analysis of the data consisting of 32 independent reflections in *p6mm* Patterson symmetry is shown in Fig. 3.11. The map has three dominant peaks and these were fitted with Mg atoms. This model is consistent with the epi-Mg structure (HT phase) and kinematical refinements to the diffraction data yielded a χ value of 1.58 using the bulk Mg and O atoms. The data set used in this analysis was obtained from a thicker region of the sample and hence is unsuitable for further charge density refinements. The results of this study are in discord with those of the

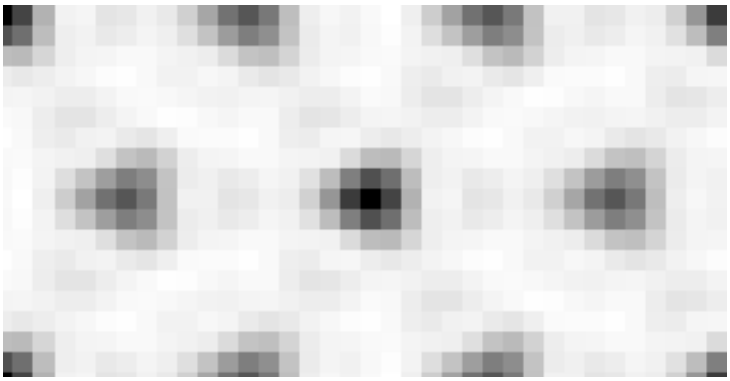

Figure 3.11. Direct methods scattering potential map for the MgO (111)-2x2 surface. The centered unit cell is shown in the figure.

previous studies, which also are mutually inconsistent. Presently, the HT phase was produced by annealing in O_2 and is stable at air. The data from Plass et al. where the sample was annealed in a reducing atmosphere has an intensity ratio ($I_{1,1}/I_{1,0}$) of 0.668 which is closer to the LT phase while the annealing should have resulted in the HT phase. The HT phase, stable only at very low oxygen chemical potentials, transforms to octopolar structure at O_2 partial pressures over $5x10^{-5}$ torr and has a ratio of about 121. The intensity of the (1,0) reflection is very sensitive to the displacements of the sub-surface O layer. The surface Mg atoms occupy special sites forming a $\sqrt{3}$ lattice and do not contribute to this reflection. Unfortunately, Finocchi et al. do not give the atomic positions of any of their structures (LT and HT) or the details of the heating mechanism employed in their study, rendering it difficult to reconcile the apparent discord. More careful experiments in controlled atmospheres are necessary to resolve these disagreements.

CHAPTER 4

Reconstructions on NiO(111) Surface

4.1. Introduction

Nickel oxide is a first-row transition metal monoxide which is used in a variety of applications, including exchange coupling in giant magnetoresistive sensors (Soeya et al., 1995), in fuel cells (Granqvist et al., 2003) and gas sensors (Hotovy et al., 2002). It also serves as a catalyst for various reactions, such as reduction of NO_x, desulphurisation of hydrocarbons and photocatalytic production of hydrogen from water (Lee et al., 2001). In the ground state it crystallizes in the rocksalt NaCl structure and exhibits antiferromagnetic ordering of type 2 (Roth, 1958), with each Ni ion having 2 unpaired electrons. The AF_2 structure is shown in Fig. 4.1, with adjacent (111) sheets of similar spin Ni ions. This spin configuration has two components, both due to the non-local exchange interaction between Ni electrons. The direct exchange interaction between nearest neighbour Ni ions favours pairing of spins to lower the energy. However, a much stronger interaction comes from the super-exchange between the next-nearest neighbour Ni ions (Terakura et al., 1984; Towler et al., 1994; Castell et al., 1997). The hybridization of the O 2p and Ni 3d states, i.e. covalent bonding between the Ni and O, is stronger than the coupling of the d-d states between nearest neighbour Ni ions and opposite

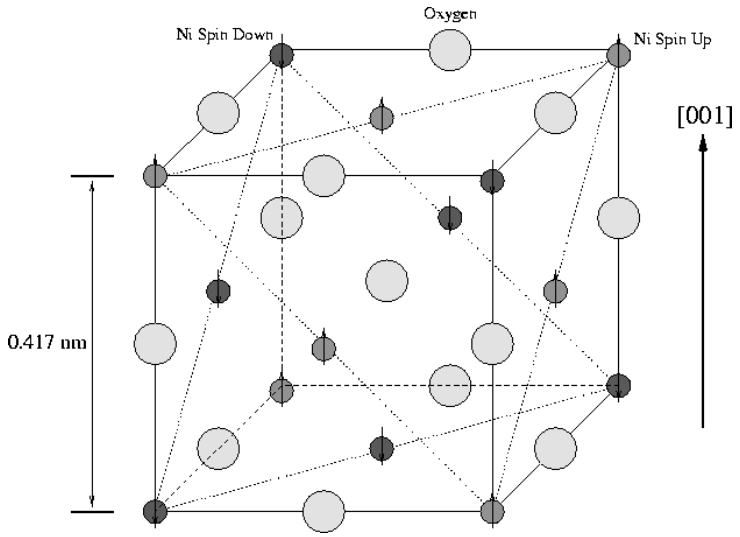

Figure 4.1. Atomic structure and spin ordering in bulk NiO

spin next-nearest neighbour ions are energetically favoured. This makes the anti-ferromagnetic spin structure the ground state of NiO. Below the Neél temperature of 523 K, the magnetic ordering is accompanied by a slight orthorhombic distortion characterized by a=4.17 $\mathring{A}$ and α=90.044 °.

In a purely ionic picture of NiO the Ni^{2+} ions have a partially filled d shell in a $3d^8$ ground-state configuration. According to conventional band-theory this should result in metallic behaviour, yet NiO is an insulator with a bulk band gap of 4.3 eV (Sawatzky and Allen, 1984). Mott (1974) proposed that the band gaps in these materials were due to strong on-site repulsion between the d-electrons of the metal ions. Coulomb repulsion between the d-electrons localized on the metal ions increases their effective band volume and produces a pseudo-filled band. Depending on the type of approximation used in an *ab initio* calculation, the

ground state of NiO is predicted to be a metal (LDA, nonmagnetic state), a 0.4 eV band-gap Mott insulator (LSDA, antiferromagnetic state), a 1.0 eV band-gap Mott insulator (GGA, antiferromagnetic state) or a 3.0 eV band-gap charge-transfer insulator (LSDA+U, antiferromagnetic state). Dudarev et al. (2000) found that the structure factors evaluated using the GGA and the LSDA+U approach agree best with accurate electron diffraction measurements. This study also found the degree of covalent bonding in NiO (determined experimentally) to be smaller than that predicted by theoretical calculations. More recently, *ab initio* calculations using LSD with self-interaction correction (SIC-LSD) report better agreement with experimental exchange coupling constants for bulk NiO (Ködderitzsch et al., 2002). Despite numerous experimental and computational studies, there is not widespread consensus on the electronic structure of bulk NiO.

Despite having the same rocksalt structure with six-fold coordinated cations and anions, MgO and NiO exhibit different habit planes during crystallization from melt. While pure MgO reflects the underlying lattice in its morphology by forming cubic crystallites, NiO does not. Experimentally, NiO is observed to express {111} faces in the morphology either in the form of an octahedron or a cuboctahedron (Ford and Dana, 1958). Experimental studies on the (111) surface have identified ($\sqrt{3}$x$\sqrt{3}$R30°)(Gajdardziska-Josifovska et al., 2002) and (2x2) reconstructions (Ventrice et al., 1994). In this chapter, the results from TEM studies of these surface structures and the morphological changes of the surface during the transition

of one phase to other are presented. First principles density functional (DF) calculations described in this chapter were carried out by Prof. L. D. Marks (WIEN, full potential).

4.2. Sample Preparation and Surface Morphology

Highly pure NiO single crystals used in this study were grown in a novel electric-arc furnace using the Verneuil technique (Merkle et al., 1985). TEM samples were made from 3 mm discs cut from (111) oriented single crystals using standard techniques outlined in Chapter 2. The samples were subsequently annealed in a tube furnace under flowing O_2 at temperatures in the range of 950°C - 1150°C to anneal out the ion-beam damage and to obtain various surface reconstructions. Annealed NiO samples were introduced into SPEAR and studied using a Hitachi UHV-H9000 300 keV TEM. Before discussing the findings of this study, it is important to emphasize that this study is different from other studies of vicinal surfaces (Jeong and Williams, 1999; Shenoy et al., 1998; Frohn et al., 1991; Arenhold et al., 1998). The difference is an unavoidable result of the standard TEM sample preparation procedure that involves the creation of a spherical depression. Thus the sample contains a range of miscut angles along all azimuthal orientations. While this gives us the ability to study a variety of vicinal surfaces in a single sample, the angle or the orientation of the miscut cannot be quantified accurately.

Figs. 4.2a & 4.2b show the diffraction pattern and bright field image obtained from a sample annealed at 950°C. The surface exhibits extended faceting with

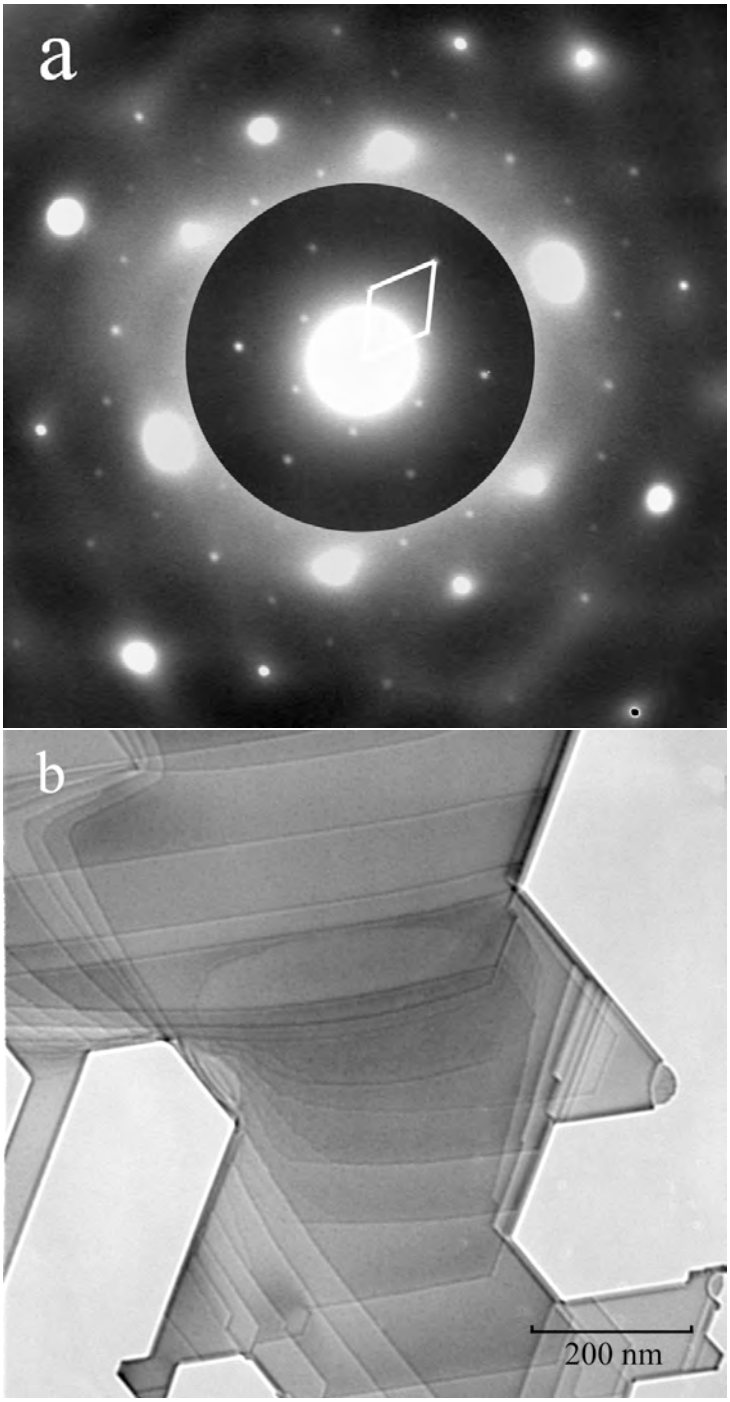

Figure 4.2. (a) Diffraction pattern from sample annealed at 950°C. The unit cell of the ($\sqrt{3}$x$\sqrt{3}$R30°) reconstruction is outlined. (b) Bright field image from the same surface showing step bunches and terraces.

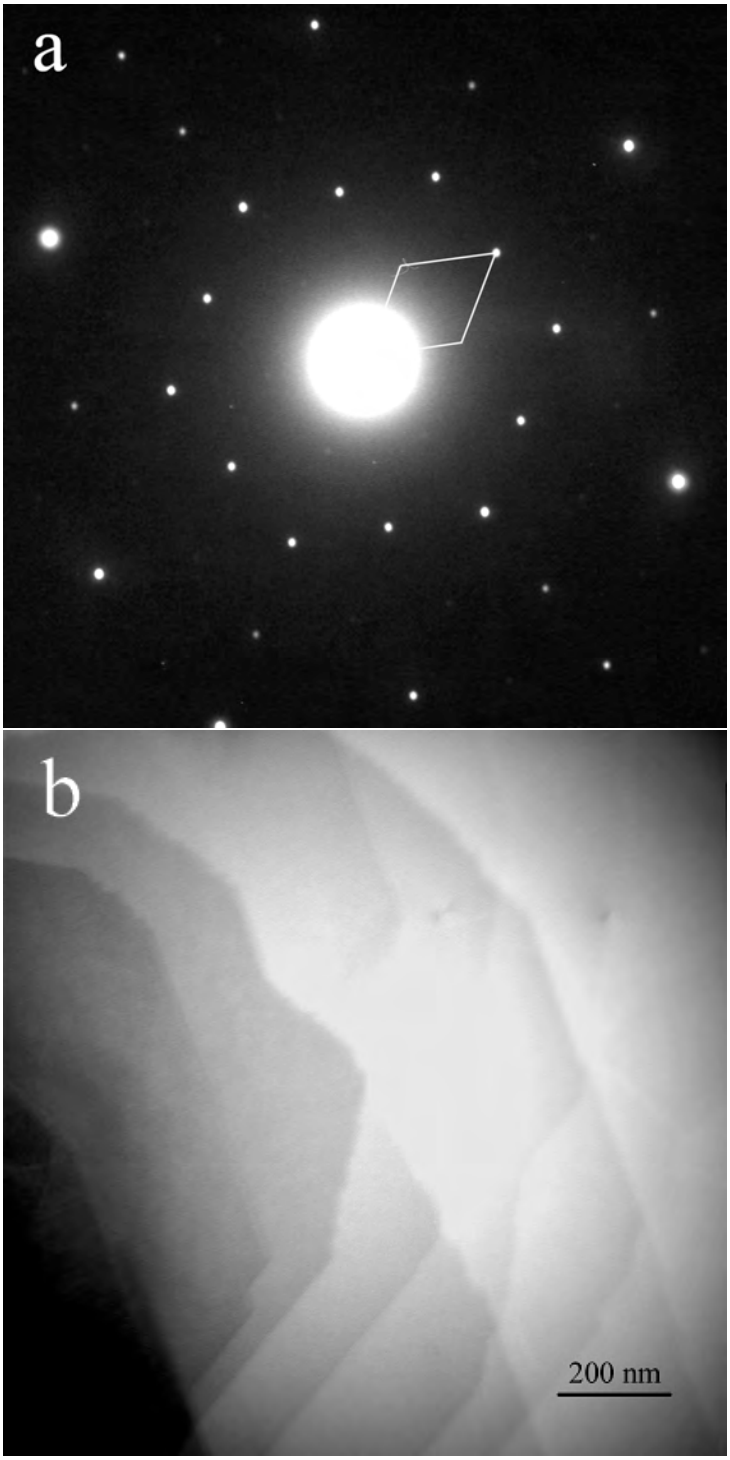

Figure 4.3. (a) Diffraction pattern from sample annealed at 1150°C. The (2x2) surface unit cell is outlined. (b) Bright field image showing the surface morphology of the surface.

step bunches and the terraces have NiO (111)-$\sqrt{3}$x$\sqrt{3}$R30° reconstruction. The steps are winding, i.e. the kink density is relatively high, and the "flat" terraces are quite large, almost 200 nm wide. Another interesting feature in this image is the nature of the edge of the sample - the profile surfaces are very well ordered and consist of {110} planes. The step facets for the most part are parallel to these crystallographic planes and hence we expect the facets in step bunches to be {110} planes. Also supporting this hypothesis is the fact that the (110) surface in rock-salt oxides is non-polar. Upon annealing the same sample at a higher temperature of 1150°C the overall surface morphology does not change significantly. The surface still comprises step bunches and wide terraces, the only difference being that the terraces now have NiO (111)-2x2 reconstruction. Figs. 4.3a & 4.3b show the structure and morphology of this surface. Again the steps run along the $< 110 >$ directions and the kink density is relatively high. These observations are consistent with previous studies on other oxide systems like MgO (Subramanian et al., 2004), SrTiO3 (Erdman and Marks, 2003). These systems exhibit a variety of reconstructions with periodicities that usually increase with temperature, with little change in surface morphology.

Samples annealed at 1050°C to study the transformation between the two surface phases reveal a startling morphology. Figs. 4.4a & 4.4b elucidate the nature of the process. The diffraction pattern, in addition to the spots from the ($\sqrt{3}$x$\sqrt{3}$) reconstruction, shows extended streaking along $< 110 >$ directions. This implies the presence of a continuous range of periodicities normal to these directions. Since

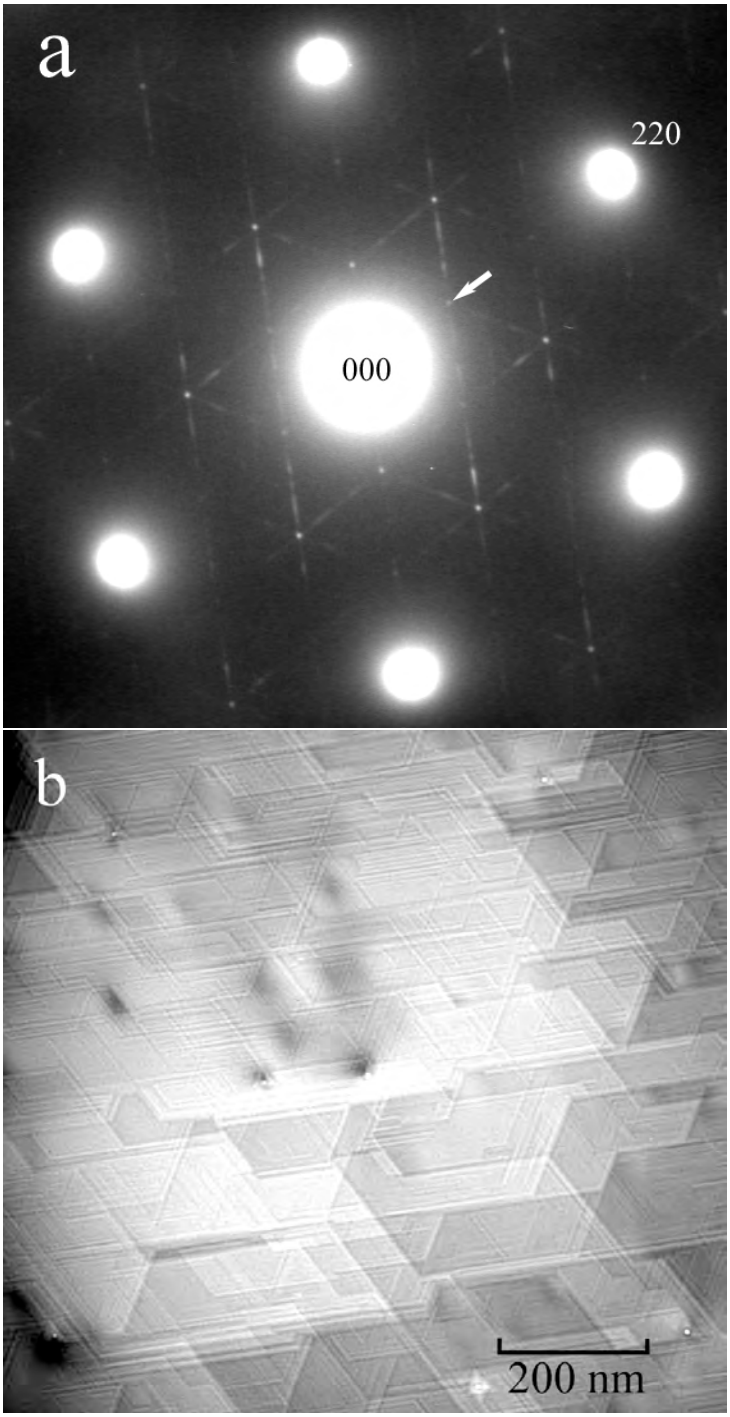

Figure 4.4. (a) Diffraction pattern from sample annealed at 1050°C. Diffraction spot from the ($\sqrt{3}$x$\sqrt{3}$) reconstruction is arrowed for reference. b) Dark field image from the surface using the (220) reflection.

it is impossible to construct a structure by modulating the surface unit cell to accommodate the various periods in six equivalent directions, the only viable option is to consider an ordering of surface steps. Indeed, a high-resolution dark field micrograph of the surface confirms this hypothesis. The micrograph suggests that the surface comprises step bunches which are separated by sloped "terraces" which have a periodic ordering of steps that are a few unit cells high. This can be seen more clearly in Fig. 4.5, an SEM image from the same TEM sample. In addition to pseudo-ordering of steps the isolated kinks present in the in the steps have coalesced to form a facet and step edges are very straight over length scales of 500 nm. This behaviour is contrary to what is what one would expect from energetic or entropic considerations (Jeong and Williams, 1999). Fig. 4.6 is a diffraction pattern where the (2x2) phase can be seen alongside the parent ($\sqrt{3}$x$\sqrt{3}$) phase. The spots from the (2x2) phase do not show any streaking while the ($\sqrt{3}$x$\sqrt{3}$), (1x1) and the bulk spots display streaking (The ($\sqrt{3}$x$\sqrt{3}$) phase has spots that overlap with these spots). Hence we conclude that the surface with the novel step structure transforms to the (2x2) phase at higher temperatures.

Surface morphology is key factor in a number of technologically relevant processes, for example, catalysis and thin film growth. The present study has identified an interesting material system to study the effect of the interactions between surface steps and reconstructions. All the phases reported above are consistently reproducible in the same sample and even in any given sample, the morphology is similar in most of the electron transparent regions around the hole. These observations

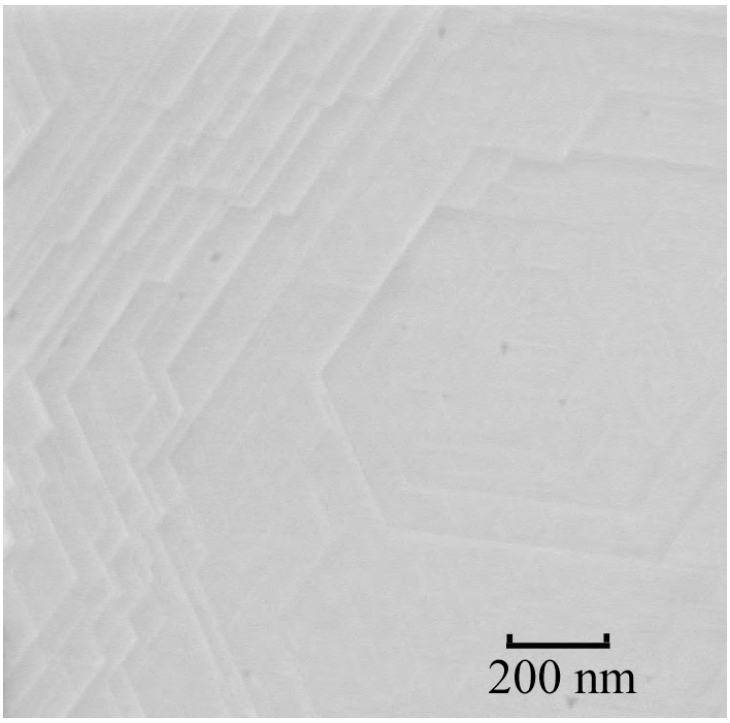

Figure 4.5. Scanning Electron Micrograph from a TEM sample annealed at 1050°C showing the surface morphology.

strongly suggest that there is a fundamental thermodynamic phenomenon at work which has minimal azimuthal anisotropy. Our present understanding of crystal morphology is based on the widely accepted theory of equilibrium faceting of crystals. The basic premise of this theory is to formulate the surface free energy as a function of surface orientation and alongside temperature, from which a Wulff construction would yield the orientation of the stable facets. This simple model has been made more effective by the addition of terms to describe the various step interactions that are expected to be present in vicinal surfaces (Marchenko, 1981). A variety of novel surface phenomena are reported in literature, based

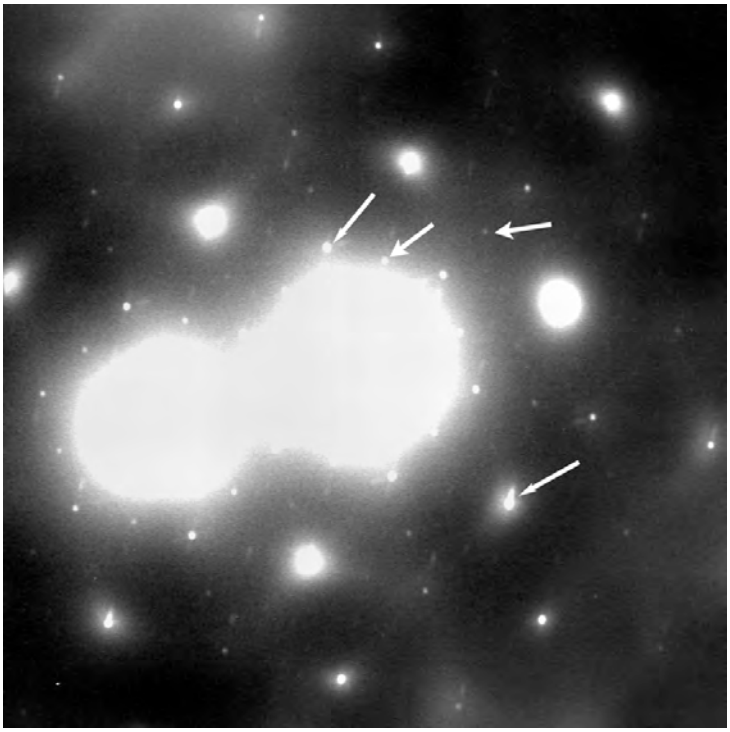

Figure 4.6. Diffraction pattern from a sample annealed at 1100°C showing both the (2x2) and ($\sqrt{3}$x$\sqrt{3}$) reconstructions. The 2x2 spots are marked by arrows with wider heads and ($\sqrt{3}$x$\sqrt{3}$) spots are marked by narrow heads.

on both experimental and theoretical studies (Jeong and Williams, 1999) and are explained by considering various types of step-step interactions, short-range attraction (Shenoy et al., 1998), medium-range attraction (Frohn et al., 1991) and long-range attraction (Arenhold et al., 1998) to name a few. In addition to these interactions, the presence of a reconstruction on the terraces between steps adds another variable to the surface morphology problem.

One interesting hypothesis to explain the ordering of steps stems from the orientation of the ($\sqrt{3}$x$\sqrt{3}$) phase w.r.t the step edges, namely $< 110 >$ directions.

Since the unit cell for the ($\sqrt{3}$x$\sqrt{3}$) phase is rotated by 30° from the step edge, every step edge can accommodate only half a unit cell. Hence every terrace must consist of an even number of unit cells normal to the step. Such "magic vicinals" have been predicted theoretically (Bartolini et al., 1989) and observed experimentally (Yoon et al., 1994) only in the case of vicinal noble metal surfaces. This however does not explain why the step-bunched morphology is observed at lower temperatures. Nevertheless, the fact that the phenomenon is observed with only the ($\sqrt{3}$x$\sqrt{3}$) reconstruction on narrow terraces suggests that the reconstruction plays an integral part in determining the surface morphology. The atomic structures of the (2x2) and the ($\sqrt{3}$x$\sqrt{3}$) reconstructions are discussed in the following sections. We find that the two surfaces have very different stoichiometries, with the the lower temperature ($\sqrt{3}$x$\sqrt{3}$) phase being cation-deficient and the higher temperature (2x2) phase being anion deficient. This changes the electron density distribution at the surface which could play an important role in the bringing about the observed step ordering. A recent study on TaC surfaces attribute the attractive interaction between steps to the electronic charge redistribution at the step (Zuo et al., 2001). Knowledge of the atomic structure of these surfaces and heights of the surface steps could provide valuable information that can be used in modelling the nature of the interactions between these steps. Atomic force microscopy was attempted to recover step height information but the step structure could not be resolved. This is because the terrace widths are on the order of tens of nanometers and the radius of standard AFM tips are of the same magnitude. STM remains

the only viable technique for this study. Even though NiO is an insulator with a 4.3 eV bandgap at room temerature, elevated temperature (∼200°C) STM studies have been successfully conducted on the (100) surface of NiO and can be easily extended to the (111) surface (Castell et al., 1997). This is an interesting problem for future studies on this surface. To the best of my knowledge, there are no studies in literature that report a reversible transformation between a step-bunched morphology to a regularly-spaced step morphology for any surface.

4.3. Fitting the bulk charge density

For the density fitting process, going beyond a neutral-atom model requires a reasonable model for the bulk NiO structure factors about which to perturb. Unlike the case of MgO, the number of studies of the charge density in bulk NiO are limited and accurate structure factors are available only for seven reflections (Dudarev et al., 2000). Hence WIEN2k calculations were performed for the bulk using the LDA+U formalism and the resulting theoretical density was fitted with spherical Ni and O atoms. The published wavefunctions of Ni and O^- were used as the basis set for this fitting process (Su and Coppens, 1998). The electron density in NiO, unlike MgO, is not well aprroximated by spherical atomic densities. A prior electron diffraction study found that the charge density in bulk NiO is more concentrated around atomic nuclei. This study also found that the electron density between Ni and O ions was reduced. This non-spherical d-electron distribution was modeled using two Gaussian features along the Ni-O bond directions. The

Table 4.1. Parameters from the bulk fitting of LDA+U densities. Refer to text for more details

Atom/Orbital	Relaxation($\kappa - 1$)%	Occupancy
Ni (3d)	3.91	10.56
Ni (4s)	28.01	0.72
O (2s)	-4.36	1.63
O (2p)	0.92	5.68
	Depletion region parameters	
position(x $a_0/2$)	size ($\mathring{A}^2$)	occupancy(e^-)
0.113	0.809	-0.162
0.196	3.261	-0.269

position of these features along the bond axis as well as their diffuseness (i.e. size) and their occupancies were allowed to vary. The other variables in the fittting process were the relaxation and occupancies of the Ni 3d/4s and O 2s/2p orbitals. The relaxations of all other orbitals in both atoms were held frozen at unity. The parameters for this fit are listed in Table. 4.1, and primarily represent the d-electron holes. The magnitude and diffuseness of the depletion region further from the Ni atom is larger than the other region, and the two together approximate a d-orbital. This is consistent with previous DFT and electron diffraction studies that found a suppression of covalent bonding in bulk NiO due to electron correlation effects (Dudarev et al., 2000). This fit represents a bulk reference state of ± 1.3 for Ni and O respectively.

4.4. NiO(111)-$\sqrt{3}$x$\sqrt{3}$R30° surface

The NiO(111)-($\sqrt{3}$x$\sqrt{3}$) surface has been reported in literature only once and the surface was found to be very stable (Gajdardziska-Josifovska et al., 2002). The reconstruction was recorded to endure months of air exposure and was found to be resistant to cold nitric acid and even 10 minutes of plasma cleaning in O_2/Ar mixture. There are no reports on the atomic structure of the surface until now. In the current study, TED data was obtained from an exposure series of 16 negatives from which the intensities of 462 surface reflections were measured. After weighted symmetry averaging, this results in 33 independent reflections for *p6mm* patterson symmetry. Direct methods were used to solve the structure in *p3*, *p3m1* and *p31m* plane groups, although it was quickly apparent that the intensity distribution was very similar to that previously found for MgO (Subramanian et al., 2004). In the case of NiO, displacements from bulk positions were detected only for the top two layers as seen in the direct methods scattering potential map. The structure has only one free positional variable, namely the x-coordinate of the second layer O atoms and it was refined to 0.308 (The unit cell for the reconstructed surface is hexagonal with $a = b = 5.107\mathring{A}$). The structure of this surface is very similar to that of the MgO(111)-($\sqrt{3}$x$\sqrt{3}$) surface underscoring the importance of the octopolar motif as a fundamental structural unit in polar oxide surfaces. We have identified the same motif in various reconstructions on the polar SrTiO3-(111) surface, which is structurally very different from MgO/NiO.

Table 4.2. Results of fits to the NiO(111)-$\sqrt{3}$x$\sqrt{3}$R30° surface charge density. The occupancies of the various atomic orbitals and the depletion regions (q_1 and q_2) are given in e^-

	Ni		Depletion		O		
Fit	3d	4s	q_1	q_2	2s	2p	χ/R
1	2	8			2	4	1.27/.143
2	0.72	10.56	-0.16	-0.27	1.63	5.67	1.33/0.123
3	0.72	10.56	-0.16	-0.27	1.57	5.50	1.73/0.199
4	0.83	11.20	-0.16	-0.27	1.52	5.31	1.03/0.081
5	0.72	10.56	-0.11	-0.19	1.52	5.31	1.03/0.078

The charge density of the NiO(111)- surface charge density was fitted following an approach similar to the one adopted in the previous section and the results are tabulated in Table. 4.2. The surface diffraction data is fitted reasonably well with neutral atoms (fit 1) or bulk atoms (fit 2). Imposing the charge neutrality constraint while using the bulk Ni atom results in a significantly worse fit (fit 3). In fit 4, the depletion regions around the top Ni atom were held frozen and the occupancies of the 3d and 4s orbitals were allowed to vary. This resulted in a significant improvement in the fit both in terms of the R-factor and the χ-value. A very similar fit was obtained when the occupancies of the Ni 3d/4s orbitals were held constant and the depletion regions were refined. Interestingly, both fits 4 and 5, though very different in terms of the way in which the charge near the top Ni atom is partitioned, yield the same oxidation state ($\sim$0.55) for the atop Ni atom. Attempts at refining both the atomic orbitals and the depletion regions of atop Ni atom proved unstable.

The structure that we find for this surface has interesting implications with respect to the anti-ferromagnetic nature of NiO. In the octahedral field of bulk NiO, the five degenerate d-orbitals of the Ni atom split into two sets: three degenerate e_g orbitals which are lower in energy than the two t_{2g} orbitals (Cotton et al., 1995). In the purely ionic limit of Ni^{2+}, these orbitals are populated by a total of eight electrons and thus give rise to two unpaired spins in the t_{2g} orbitals. This translates to 6 "up" spins per $\sqrt{3}$ unit in a complete Ni layer(For the model that we find, the first complete Ni layer going into bulk is the third layer). Three of these spins are compensated by the "down" spins from the Ni layer immediately below (layer 5). This leaves three spins to be compensated for by the surface Ni atom. From considerations of compensation of surface polarity, the oxidation state of the surface Ni atom should be reduced to +1 and those of the second layer O atoms to -1.33. This gives the surface Ni atom one extra electron compared to the bulk Ni atom. The environment around the surface Ni atom is close to tetrahedral and for this case, the crystal field theory predicts a reversal in the energy ordering of the e_g and t_2g orbitals. This results in a $[Ar]3d^74s^2$ configuration for this atom which gives 3 "down" spins for every $\sqrt{3}$ unit. Thus the resulting structure has no net magnetic dipole moment normal to the surface (in addition to the electric dipole moment). Computational studies using full potential WIEN2K DFT package are underway to verify the experimental observations.

4.5. NiO(111)-2x2 surface

NiO(111)-2x2 surface has been the subject of many experimental and theoretical studies in the last decade. It was first observed experimentally, using LEED and STM, by Ventrice et al. (1994) on NiO films grown on Au(111). In this study, the film growth was accomplished by depositing Ni onto a Au substrate held at 300°C in a UHV chamber backfilled with O_2 at 2x10^{-6} mbar. *In situ* STM images showed a stable reconstruction characterized by relatively flat (corrugation <0.2 $\mathring{A}$) terraces with a step height of ∼2.4 $\mathring{A}$ and several missing-atom point defects. The images showed features that were interpreted as micropyramidal structures (three-atom clusters with the atom of opposite charge located above each cluster) on the surface; however, the authors were not able to conclude whether the micropyramids were oxygen- or nickel-terminated. The next study was carried out by Barbier et al. (2000a) using both a single crystal and a 5ML thick NiO(111) film grown on Au(111) surface. The authors concluded that the single crystal surface was terminated with a Ni-terminated octopolar reconstruction and double steps. The surface of the thin film sample, owing to the non-equilibrium growth conditions, was determined to accomodate a mixture of both Ni- and O-terminated octopolar reconstructions (and hence single steps). The diffraction data from this thin film sample was analyzed by Erdman et al. (2000) and a new single-phase structure was proposed for the surface. The new hybrid structure is characterized by alternating close-packed layers of nickel and oxygen atoms. The top surface

layer is Ni-terminated, with 3/4 of the Ni atoms missing, the next O-layer is completely full. The third Ni layer has 1/4 of its atoms missing. This surface is non-stoichiometric, unlike the octopolar surfaces, and is cation deficient. Most recently, the surface was studied again by Barbier et al. (2000b) using single crystal samples annealed —texitiex situ followed by *in situ* UHV anneals at an O_2 partial pressure of 10^{-5} mbar. This time the authors report a two phase surface comprising of O-terminated octopoles and O-capped spinel, with a continuous phase transition between the two phases depending on the degree of reduction. Interestingly enough, both the proposed structures are stoichiometric, even though they form under oxidizing and reducing environments, respectively.

In the present work, the NiO(111)-2x2 reconstruction was obtained on single crystal NiO samples as described in the previous section. TED data obtained from this sample comprised 836 surface reflections which upon symmetry averaging yielded 77 independant reflections (in *p6mm*). Like in the case of MgO (111)-2x2 surface, the Direct Methods analysis yielded maps with three prominent peaks. Nickel atoms assigned to these peaks form a $(\sqrt{3}\text{x}\sqrt{3})$ lattice. In retrospect, this is evident in the intensity ordering observed in the diffraction pattern: the strongest spots in the surface diffraction pattern should also lie on the $(\sqrt{3}\text{x}\sqrt{3})$ lattice. The positions of the oxygen atoms were obtained through difference maps. Starting from the bulk fits described in previous section, the charge density of the surface was refined. The three surface nickel atoms and one of the four second-layer oxygen atoms are at special sites and do not have any positional degrees of freedom. Hence

Table 4.3. Atomic coordinates of the various species on the NiO(111)-2x2. $a = b = 5.897\mathring{A}\gamma = 120°$.

Atom	x	y
Ni1	0	0
Ni1	1/3	2/3
Ni1	2/3	1/3
O1	0	0
O1	0.493	0.507

structure has only one free positional variable (the other inequivalent O atom in the second layer has to lie on the mirror along the long diagonal). The refined positions of the surface species did not vary much for the various fits and are listed in Table. 4.3.

Fitting the surface diffraction data with neutral atoms (Fit 1 in Table. 4.4) gave a χ value of 1.42 while with bulk Ni and O atoms the χ was 1.74. Transferring the model used for bulk fitting to fit the surface density, the occupancies of the gaussian depletion features were allowed to vary in addition to occupancies of the spherical oxygen 2s/2p orbitals and the spherical components of the Ni 3d/4s orbitals. The six "depletion" features which are part of the bulk Ni atom lie along the $< 100 >$ type directions and were transferred to the surface by projecting them along the [111] direction. Charge neutrality was enforced and the relaxations of all the orbitals of all atoms along with the size and position of the depletion regions were held constant. All attempts at varying the occupancies of the two Ni atoms on threefold sites yielded unreasonable numbers and poor fits. For subsequent fits, these two atoms were constrained to be identical to the bulk Ni atom. The bonding

Table 4.4. Results of fits to the NiO(111)-2x2 surface charge density. The occupancies of the various atomic orbitals and the depletion regions (q_1 and q_2) are given in e^-

	Ni1		Depletion		O1		O2		
Fit	4s	3d	q_1	q_2	2s	2p	2s	2p	χ/R
1	2	8			2	4	2	4	1.42/0.076
2	0.72	10.55	-0.16	-0.27	1.63	5.68	1.63	5.68	1.74/0.16
3	4.56	6.29	-0.16	-0.27	1.46	5.09	1.68	5.87	1.08/0.038
4	2	8			1.72	5.99	1.60	5.56	1.39/0.055

environment of the other surface Ni atom is very different since it is directly above a sub-surface O atom (which is the only atom it is bonded to). The depletion region around this Ni atom was modified to resemble a d_{z^2} orbital directed at the O atom below. The magnitude of the depletion region was held constant and the occupancies of Ni 3d and 4s orbitals were allowed to vary. If the orbital occupancies are used to compute the oxidation state, then the atop Ni atom turns out to be neutral. When the same fit was attempted with a spherically symmetric neutral Ni atom without depletion regions, the resulting fit is much poorer (fit 4). This underscores the sensitivity of the experimental data to the differences in the electron density surrounding the atop Ni atom.

The present study has shed some light on some of the unresolved issues with the NiO (111)-2x2 surface. The reconstruction has been obtained under very different annealing conditions and despite having the same unit cell mesh, the atomic structures are different. The model that we propose for this surface is metal-rich

and can be viewed as a (111) termintaion of Ni_3O_4 spinel. Incidentally, the metal-deficient hybrid structure proposed by Erdman et al. can also be viewed as a spinel termination of the surface (albeit a different one). Ni_3O_4 is not stable as a bulk phase but has been identified to grow epitaxially on NiO surfaces under electron irradiation (Buckett, 1991). The unit cell of the spinel phase is exactly double that of NiO (thereby forming a 2x2 overlayer) and the spinel structure can be modified to accomodate a wide range of stoichiometries without introducing point defects. The possibility of finding other spinel terminations is something that needs to be explored through further experimentation.

CHAPTER 5

Reconstuctions on $SrTiO_3$(110)

5.1. Introduction

$SrTiO_3$ is mixed metal oxide with a perovskite structure and and is the most studied member in this class of materials. It is a technologically useful material with applications in photoelectrolysis, surface chemical reactions, and as a substrate for the growth of high-T superconductors. Recently the semiconductor industry has discovered $SrTiO_3$, which is witnessed in its use as thin film gate oxide instead of SiO_2 and also as a buffer layer for growth of GaAs thin films on Si (McKee et al., 1998).

The crystal structure of bulk $SrTiO_3$ is surprisingly simple for a mixed-metal oxide of multiple-valence cations. The perovskite structure comprises a simple-cubic lattice of strontium with titanium at the body-center and oxygens at face-centers. The bulk lattice parameter is 3.905 $\mathring{A}$ and along the (110) direction there are two possible bulk terminations : (a)A positively charged SrTiO layer or (b) a negatively charged O_2 layer with a net charge of ± 4 per 1x1 cell (see Fig 5.1). The dimensions of the 1x1 surface unit cell are 3.905 $\mathring{A}$ along the [100] direction and 5.522 $\mathring{A}$ along the [110] direction. While there is an increasing number of studies

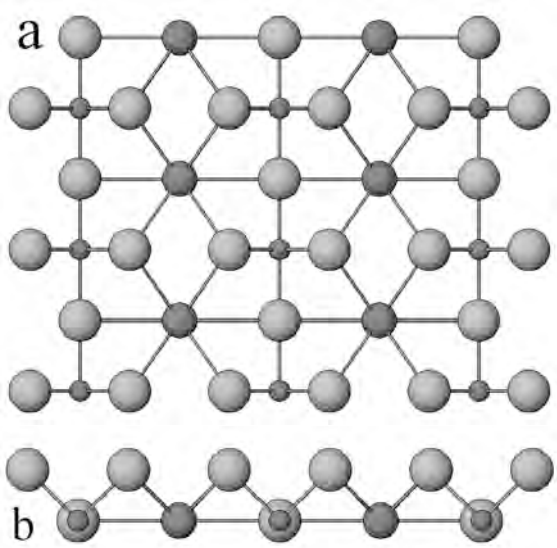

Figure 5.1. Bulk structure of $SrTiO_3$ (a) along the [110]direction (b) along [001] direction. The horizontal direction in both cases is $[1\bar{1}0]$. The lighter circles are O, small dark circles are Ti and large dark circles are Sr.

of the (001) surface, there are only a few reports about the detailed topographic and electronic structure of the (110) surface.

Thermal etching of SrTiO3 (001) and (110) surfaces at elevated temperatures has been studied extensively various researchers (Tomashpolskii et al., 1981; Henrich, 1983). The general consensus is that annealing at temperatures in the range of 850°-1150°C results in the preferential evaporation of SrO from the surface. X-ray photoelectron spectroscopy studies have been carried out on $SrTiO_3$ (110) and (001) surfaces reduced in UHV at temperatures of 800°C and 1000°C (Aiura et al., 1994a,b). When reduced at 800°C, the (110) surface exhibits a metallic state with a sharp Fermi cut-off and a broad state around ∼1.1eV below the Fermi level. The

1000°C anneal results in significant weakening of the metallic state with only the 1.1eV state remaining in the band gap region. Equivalent studies on the (100) surface show only a broad state at ∼1eV below E_F. This points to some similarities in the coordination environment of the surface Ti atoms on (100) and (110) surfaces reduced at 1000°. A theoretical study of reduced SrTiO3 by Tsukada et al. (1983) found that the highest occupied molecular orbital induced by oxygen vacancies is broadly distributed around Ti atoms and extends into the vacuum region. This result is used by Aiura et al. to explain the metallic state found in the (110) surface reduced at 800C as being caused by an overlapping of the Ti^{2+} states (on the ridges running along the [001] direction) along the [l10] direction. The disappearance of this metallic state at the (110) surface reduced at 1000°C is attributed to the formation of TiO_2 (100)/(010) facets with a larger spacing along the [110] direction precluding such an overlap. Thus the "microfacetted" surface was inferred for the (110) surface which was subsequently used by Bando et al. (1995) to explain their STM observations. In XPS measurements of both the (100) and (110) surfaces, Sr 3d features did not show any variations, suggesting that there is almost no Sr on the reduced surfaces. This is consistent with previous studies on the atomic structure of the $SrTiO_3$ (100) surface (Erdman et al., 2002, 2003)

The atomic structure of $SrTiO_3$ (110) surfaces prepared by UHV annealing at temperatures around 1000°C was studied by Brunen and Zegenhagen (1997) using LEED and STM. Table. 5.1 lists the sample preparation conditions and the

resulting surface reconstuctions. The authors report a strong modulation of the intensities of the LEED spots with many of them missing for most of the reported structures. This strongly suggests that the surface is not fully ordered or equilibrated under the annealing conditions employed. This hypothesis is supported by the STM observations of the reported structures which find that the sample surface is faceted with widely distributed small rectangular holes. High-resolution STM images of sample A showed strips running along the (001) direction while those of samples C and E showed stripes running along $[1\bar{1}0]$ direction. While stripes along the [001] direction can be explained by the microfaceting model, those along [110] cannot. The internal structures of stripes in both directions were not periodic which proves the lack of surface ordering.

5.2. TEM studies of the $SrTiO_3$(110)-3x4 surface

TEM samples were made from commercial $SrTiO_3$ wafers by employing standard techniques outlined in section 2. Figs. 5.2a & 5.2b show the image and diffraction obtained from a sample annealed for one hour at 950°C under flowing O_2. The diffraction pattern shows streaking only along the $[1\bar{1}0]$ direction which corresponds to a structure with well defined period only along one axis in real space, namely the $[1\bar{1}0]$ direction (A one-dimensional structure along the [001] direction in real space gives rise to streaks normal to [001] direction in reciprocal space). This is clearly seen in the accompanying bright field image which shows regularly spaced lines. This is in good agreement with previous STM studies which

Table 5.1. List surface structures observed on $SrTiO_3$(110) surface

Experiment index	Annealing treatment	Type of reconstruction
A	960°C for 2 hrs	2x5
B	900°C for 4 hrs and 910°C for 2 hrs	3x4
C	960°C 20h	4x4
D	B followed by 1120°C for 10 min	4x7
E	sputter C at 960°C for 30 min and anneal for 1h	6x4a
F	sputter C at 900°C for 1 hr and anneal for 30 min	6x4b

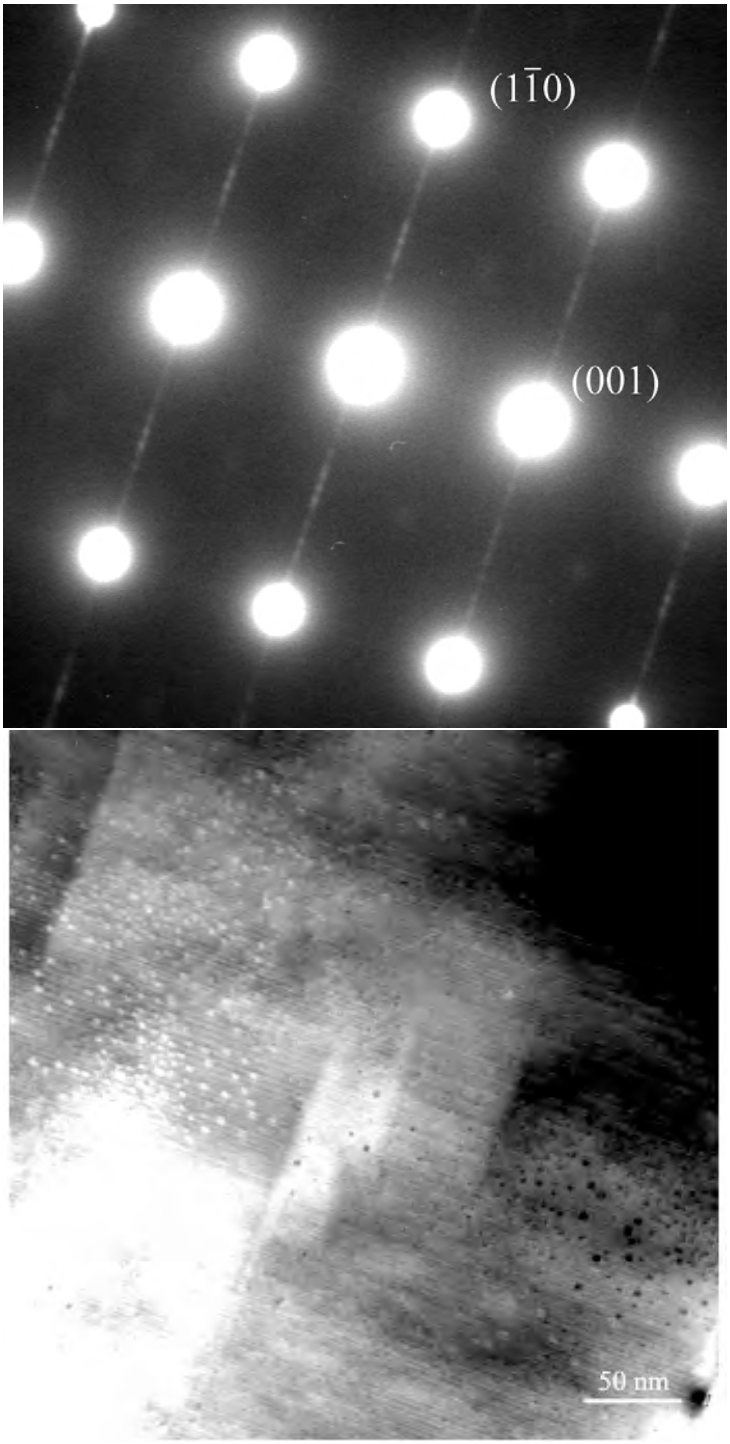

Figure 5.2. (a) Diffraction pattern from sample annealed at 950°C in O_2. Streaking along the [1$\bar{1}$0] directions is evident. b) Bright field image from the surface showing a striped structure possibly from "microfaceting".

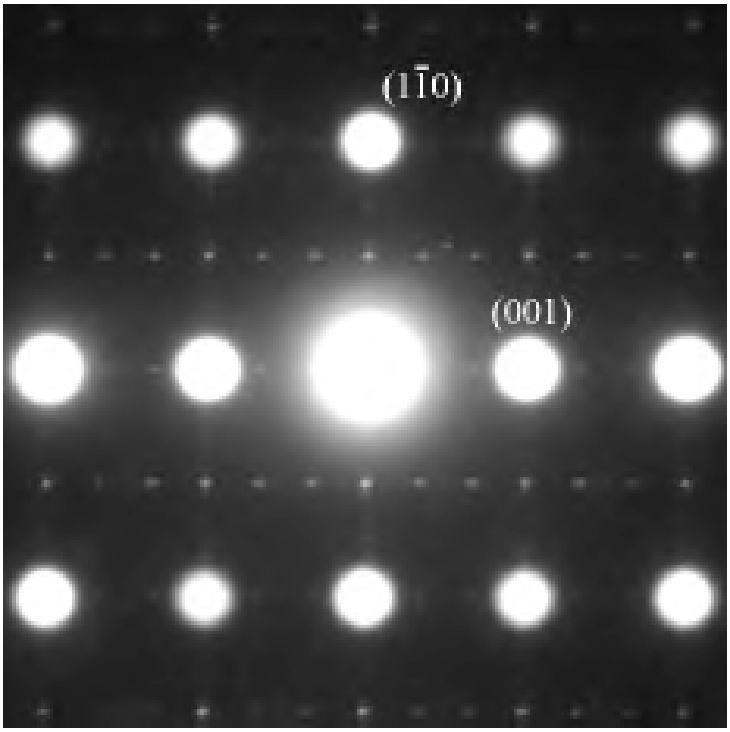

Figure 5.3. Diffraction pattern from sample annealed at 1000°C in O_2. The surface is beginning to reconstruct in two-dimensions with a x3 period along the [001] direction and a x4 period along the [1$\bar{1}$0] direction.

imaged a stripe structure running along the [001] directions in samples annealed at this temperature. Temperature and O_2 partial pressure were found to have a significant influence on the type of reconstruction obtained on $SrTiO_3$ surfaces. Samples annealed in air at a slightly higher temperature of 1000°C had the same structure while those annealed in O_2 at the same temperature started to show evidence of two-dimensional ordering (see Fig 5.3). The surface is well ordered along the [001] direction with the unit cell period increasing to three times the bulk a_{001} spacing. Along the [1$\bar{1}$0] direction, the strongest spots correspond to the

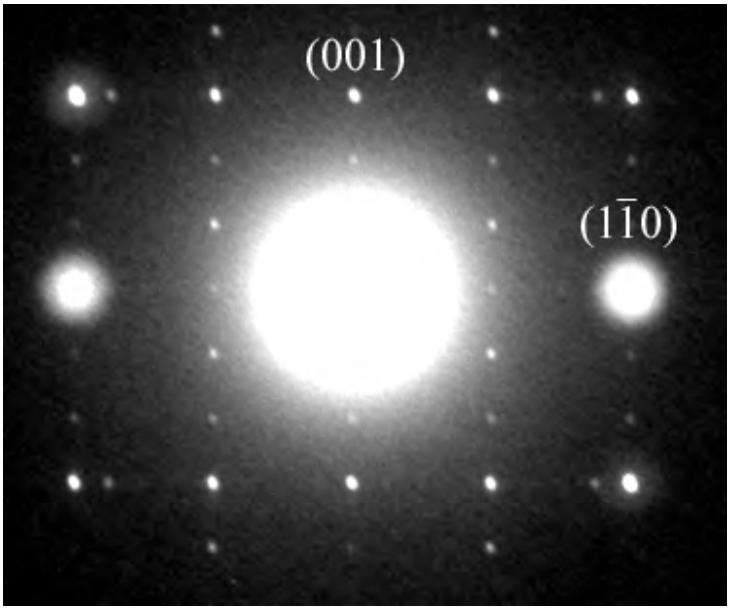

Figure 5.4. Diffraction pattern from sample annealed at 1100°C in O_2. Sharp superlattice spots indicate that the surface is completely ordered in both directions.

bulk translation, although one can see the incipient features of the formation of a larger period. Annealing at 1100°C under O_2 completes this ordering process and a (3x4) superstructure forms on the $SrTiO_4$ (110) surface. In the diffraction pattern from this surface (shown in Fig. 5.4) all the surface diffraction spots are sharp with no sign of streaks.

Surface diffraction data obtained from this comprised 158 indepedant reflections in *p2mm* symmetry. Direct methods analysis was conducted on this data set and the resulting scattering pontential map and an atomic model of the projected structure is shown in Fig. 5.5. The map shows a fragment of the surface structure and refinements are currently underway to complete the structure using standard

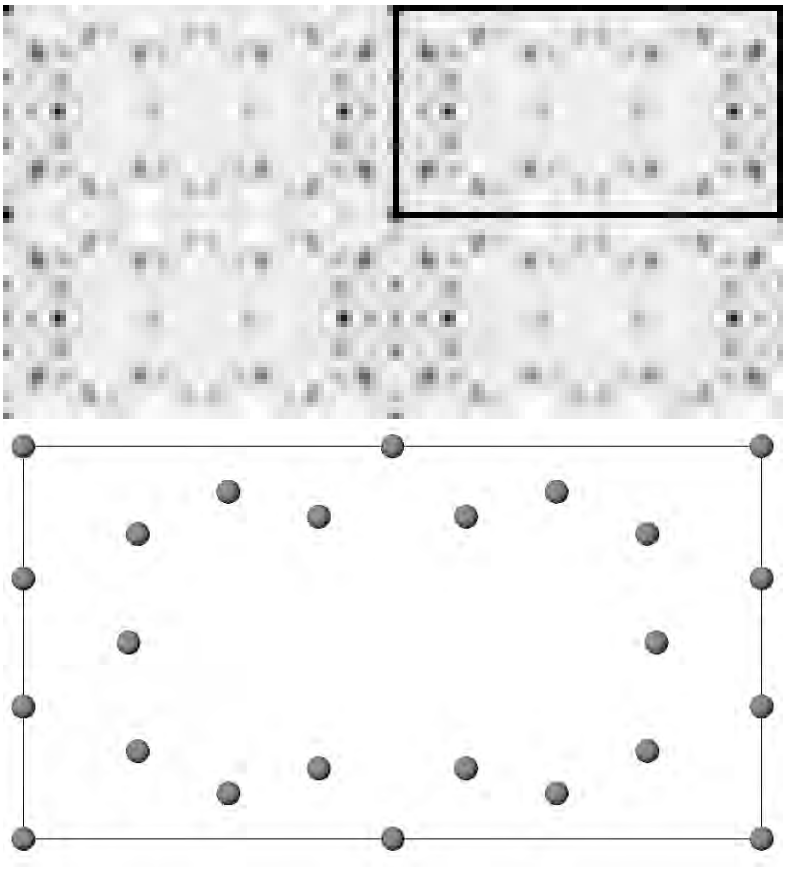

Figure 5.5. (a) Direct methods scattering potential map of $SrTiO_3$ (110)-3x4 (unit cell is outlined) and (b) Postions of the cations in the same structure. For both maps the horizontal axis is the $[1\bar{1}0]$ direction

difference map techniques. From the inital glimpses of the structure the following comments can be made about the structure:

(1) The structure that we find is consistent with STM observations of stripes running along $[1\bar{1}0]$ direction

(2) The structure has features that are similar to the $SrTiO_3$ (001)-c(6x2) surface which is obatined by annealing a (100) sample at similar temeperatures. The length of the longer axis of the unit cell for the (110) surface is 22.09 $\mathring{A}$ which is quite similar to the long axis of the the c(6x2) surface (23.43 $\mathring{A}$). The structure of the c(6x2)surface is currently under study in our group and the most recent analysis indicates a cation ordering which has a x4 translational symmetry along the longer axis similar to one observed on the (110) surface. This again is very promising since earlier XPS studies found similar electronic states for Ti atoms on both (100) and (110) surfaces annealed at these temperatures.

CHAPTER 6

Future Work

The experimental studies conducted during the course of this dissertation have served to enhance the understanding of the surface structures on polar oxide surfaces. The combination of Direct Methods applied to transmission electron diffraction data and theoretical DFT calculations for 3D surface structure determination, as well as the morphological and atomic-scale details of the structure obtained with TEM provide a multidimensional method for surface structure determination. We have also developed transmission electron diffraction as a tool to study the charge density of surfaces, which is a field that has not been broached until now. The studies of the the reconstructions on the polar (111) surfaces of rocksalt oxides MgO and NiO have experimentally verified the surface charge transfer as a stabilizing mechanism. Current experimental data in the study of these surfaces hints at the possiblity of superstructures, which, depending on annealing conditions, have identical surface unit cell meshes with different internal atomic structures. This aspect of the problem needs to be studied further by careful annealing experiments under very controlled atmospheres. The addition of a gas cell to the SPEAR has opened the door to such *in situ* experiments which can provide considerable insight into the nature of these surfaces. All oxide samples used in this

study were made by ion-milling and it is well established that this process results in preferential sputtering of oxygen from the surface. Thus the starting material for these experiments is a highly reduced sample, especially in the near surface region. Even though the results described in this study are highly reproducible within the experimental framework, it would be an interesting project to explore if these structures can be obtained on samples prepared through other techniques that do not reduce the sample surface (such as etching or wedge samples).

The present study on the NiO(111) surface has identified an interesting material system to study the effect of the interactions between surface steps and reconstructions. Our present understanding of crystal morphology is based on the widely accepted theory of equilibrium faceting of crystals. In the last few decades this theory has been extended by the addition of step interactions and surface reconstructions. From STM experiments on this surface one can obtain quantitative information on terrace widths and step-height distributions which coupled with the knowledge of the atomic structures of the terraces can be used to modelling. The only downside to this study is that it requires a special experimental setup, namely a high-temperature STM.

Another direction for future work is to study the growth of metals on reconstructed polar oxides. Metal deposition can provide charge and polarity compensation of a polar surface. The discipline of metal deposition on semiconductors and various oxides has been extensively studied but most of thse studies do not account for the substrate surface reconstructions. There are reports where small particles

are known to co-exist with surface reconstructions and the study of energetics of such a system merits further study. Again SPEAR with its UHV evaporator and interfaced TEM offers a unique experimental setup where such studies can be conducted *in situ*.

Experimental studies on the polar $SrTiO_3$ (110) surface has identified many reconstructions (3x4, 4x4, 6x4, 2x5 to name a few ..) whose atomic structures are not known. The (100) surface of this material is well documented and the (111) surface is currently being studied in our group. Filling in the experimental gap in the (110) surface studies will complete the database which can then be extended to other perovskite oxide systems.

References

Aiura, Y., H. Bando, T. Maruyama, Y. Nishihara, Y. Haruyama, S. Kodaira, T. Komeda, Y. Sakisaka, and H. Kato. 1994a. Effect of surface oxygen vacancies on electronic states of reduced $SrTiO_3(110)$ surface. *Physica C* 235-240:1009–1010.

Aiura, Y., Y. Nishihara, Y. Haruyama, T. Komeda, S. Kodaira, Y. Sakisaka, T. Maruyama, and H. Kato. 1994b. Effects of surface oxygen vacancies on electronic states of $TiO_2(110)$, $TiO_2(001)$ and $SrTiO_3(001)$ surfaces. *Physica B* 194-196:1215–1216.

Arenhold, K., S. Surnev, P. Coenen, H. P. Bonzel, and P. Wynblatt. 1998. Scanning tunneling microscopy of equilibrium crystal shape of Pb particles: test of universality. *Surf. Sci.* 417:L1160–L1165.

Bader, R. F. W. 1990. *Atoms in molecules: A quantum theory.* Oxford: Clarendon press.

Bando, H., Y. Aiura, Y. Haruyama, T. Shimizu, and Y. Nishihara. 1995. Structure and electronic states on reduced $SrTiO_3(110)$ surface observed by scanning tunneling microscopy and spectroscopy. *J. Vac. Sci. Tech. B* 13:1150–1154.

Barbier, A., C. Mocuta, H. Kuhlenbeck, K. F. Peters, B. Richter, and G. Renaud. 2000a. Atomic structure of the polar NiO(111)-p(2x2) surface. *Phys. Rev. Lett.* 84:2897–2900.

Barbier, A., C. Mocuta, and G. Renaud. 2000b. Structure, transformation, and reduction of the polar NiO(111) surface. *Phys. Rev. B* 62:16056–16062.

Bartolini, A., F. Ercolessi, and E. Tosatti. 1989. "Magic" vicinal surfaces stabilized by reconstruction. *Phys. Rev. Lett.* 63:872–875.

Benedek, R., M. Minkoff, and L. H. Yang. 1996. Adhesive energy and charge transfer for MgO/Cu heterophase interfaces. *Phys. Rev. B* 54:7697–7700.

Bengu, E., and L. D. Marks. 2001. Single-walled BN nanostructures. *Phys. Rev. Lett.* 86:2385–2387.

Binns, C. 2001. Nanoclusters deposited on surfaces. *Surf. Sci. Rep.* 44:1–49.

Blaha, P., K. Schwarz, G. K. H. Madsen, D. Kvasnicka, and J. Luitz. 2001. **WIEN2k**, an augmented plane wave + local orbitals program for calculating crystal properties (Karlheinz Schwarz, Techn. Universitat Wien, Austria) ISBN 3–9501031–1–2.

Bonnell, D. A. 1998. Scanning tunneling microscopy and spectroscopy of oxide surfaces. *Prog. in Surf. Sci.* 57:187–252.

Brese, N. E., and M. O'Keeffe. 1991. Bond-valence parameters for solids. *Acta Crystallogr. B* 47:192–197.

Brill, R. 1960. On the influence of binding electrons on x-ray intensities. *Acta Crystallogr. A* 13:275–276.

Brown, A. S., and M. A. Spackman. 1991. A model study of the kappa-refinement procedure for fitting valence electron-densities. *Acta Crystallogr. A* 47:21–29.

Brunen, J., and J. Zegenhagen. 1997. Investigation of the $SrTiO_3(110)$ surface by means of LEED, scanning tuneneling microscopy and auger spectroscopy. *Surf. Sci.* 389:349–365.

Buckett, M. 1991. Phd dissertation, Northwestern University .

Castell, M. R., P. L. Wincott, N. G. Condon, C. Muggelberg, G. Thornton, S. L. Dudarev, A. P. Sutton, and G. A. D. Briggs. 1997. Atomic-resolution STM of a system with strongly correlated electrons: NiO(001) surface structure and defect sites. *Phys. Rev. B* 55:7859–7863.

Chambers, S. A. 2000. Epitaxial growth and properties of thin film oxides. *Surf. Sci. Rep.* 39:105–180.

Chan, D. K., D. N. Seidman, and K. L. Merkle. 1995. Chemistry and structure of CdO/Ag{222} heterophase interfaces. *Phys. Rev. Lett.* 75:1118–1121.

Chang, L. D., M. Z. Tseng, E. L. Hu, and D.K. Fork. 1992. Epitaxial MgO buffer layers for $YBa_2Cu_3O_{7-x}$ thin-film on GaAs. *Appl. Phys. Lett.* 63:1753–1755.

Chiaramonti, A. 2004. Private communication .

Chiaramonti, A., and L. D. Marks. 2005. In preparation .

Chung, Y. W. 2001. *Practical guide to surface science and spectroscopy*. San Diego: Academic press.

Collazo-Davila, C. 1999. Phd dissertation, Northwestern University .

Collazo-Davila, C., D. Grozea, and L. D. Marks. 1998a. Determination and refinement of the Ag/Si(111)-(3x1) surface structure. *Phys. Rev. Lett.* 80:1678–1681.

Collazo-Davila, C., D. Grozea, L. D. Marks, R. Feidenhans'l, M. Nielsen, L. Seehofer, L. Lottermoser, G. Falkenberg, R. L. Johnson, M. Gothelid, and Karlsson U. 1998b. Solution of Ge(111)-(4x4)-Ag structure using direct methods applied to x-ray diffraction data. *Surf. Sci.* 418:395–406.

Collazo-Davila, C., E. Landree, D. Grozea, G. Jayaram, R. Plass, P. C. Stair, and L. D. Marks. 1995. Design and initial performance of an ultrahigh vacuum sample preparation, evaluation, analysis and reaction (SPEAR) system. *J. Mic. Soc. Am.* 1:267–279.

Combettes, P. L. 1996. *Advances in imaging and electron physics*. New York: New York Academic Press.

Coppens, P. 1997. *X-ray charge densities and chemical bonding*. New York: Oxford university press.

Coppens, P., T. N. Guru Row, P. Leung, E. D. Stevens, P. J. Becker, and Y. W. Yang. 1979. Electron population analysis of accurate diffraction data. 7. net atomic charges and molecular dipole-moments from spherical-atom x-ray refinements, and the relation between atomic charges and shape. *Acta Crystallogr. A* 35:63–72.

Cotton, F. A., G. Wilkinson, and P. Gaus. 1995. *Basic inorganic chemistry 3rd ed.* New York: Wiley.

Cowley, J. M. 1986. *Diffraction physics.* Amsterdam: North holland physics publishing.

Crozier, P. A., M. Gajdardziska-Josifovska, and J. M. Cowley. 1992. Preparation and charaterization of MgO surfaces by reflection electron microscopy. *Mic. Res. Tech.* 20:426–438.

Dawson, B. 1969. Significance of accurate structure factors. *Acta Cryatallogr. A* 25:12.

Dorset, D. L. 1997. The accurate electron crystallographic refinement of organic structures containing heavy atoms. *Acta Crystallogr.* A53:356–365.

Doyle, P. A., and P. S. Turner. 1968. Relativistic hartree-fock x-ray and electron scattering factors. *Acta Crystallogr. A* 24:390.

Dudarev, S. L., L. M. Peng, S. Y. Savrasov, and J. M. Zuo. 2000. Correlation effects in the ground-state charge density of mott insulating NiO: A comparison of *ab initio* calculations and high-energy electron diffraction measurements. *Phys. Rev. B* 61:2506–2512.

Duke, C. B. 1996. Semiconductor surface reconstruction: The structural chemistry of two-dimensional surface. *Chem. Rev.* 96:1237–1259.

Erdman, N., M. Asta, O. Warschkow, D. E. Ellis, K. R. Poeppelmeier, and L. D. Marks. 2002. The structure and chemistry of the TiO_2-rich surface of $SrTiO_3(001)$. *Nature* 419:55–58.

Erdman, N., and L. D. Marks. 2003. $SrTiO_3(001)$ surface structures under oxidizing conditions. *Surf. Sci.* 526:107–114.

Erdman, N., O. Warschkow, M. Asta, K. R. Poeppelmeier, D. E. Ellis, and L. D. Marks. 2003. Surface structures of $SrTiO_3$(001): A TiO_2-rich reconstruction with a c(4x2) unit cell. *J Am. Cer. Soc.* 125:10050–10056.

Erdman, N., O. Warschkow, D. E. Ellis, and L. D. Marks. 2000. Solution of the p(2x2) NiO(111) surface structure using direct methods. *Surf. Sci.* 470:1–14.

Ertl, G., and H. J. Freund. 1999. Catalysis and surface science. *Physics Today* 52: 32–38.

Finocchi, F., Antoine Barbier, Jacques Jupille, and Claudine Noguera. 2004. Stability of rocksalt (111) polar surfaces: Beyond the octopole. *Phys. Rev. Lett.* 92: 136101.

Ford, W. E., and E. S. Dana. 1958. *A textbook of mineralogy.* New York: Wiley.

Fork, D. K., and G. B. Anderson. 1993. Epitaxial MgO on GaAs(111) as a buffer layer for z-cut epitaxial lithium-niobate. *Appl. Phys. Lett.* 63:1029–1031.

Fork, D. K., K. Nashimoto, and T.H. Geballe. 1992. Epitaxial $YBa_2Cu_3O_{7-\delta}$ on GaAs(001) using buffer layers. *Appl. Phys. Lett.* 60:1621–1623.

Freund, H. J., H. Kuhlenbeck, and V. Staemmler. 1996. Oxide surfaces. *Rep. Prog. Phy.* 59:283–347.

Frohn, J., M. Giesen, M. Poensgen, J. F. Wolf, and H. Ibach. 1991. Attractive interactions between steps. *Phys. Rev. Lett.* 67:3543–3546.

Gajdardziska-Josifovska, M., P. A. Crozier, and J. M. Cowley. 1991. A $(\sqrt{3}x\sqrt{3})r30^\circ$ reconstruction on annealed (111) surfaces of MgO. *Surf. Sci. Rep.* 248:L259–L264.

Gajdardziska-Josifovska, M., R. Plass, M. A. Schofield, D. R. Giese, and R. Sharma. 2002. *In situ* and *ex situ* electron microscopy studies of polar oxide surfaces with rock-salt structure. *J. Electron Microscopy* 51(supplement): s13–s25.

Gerchberg, R. W., and W. O. Saxton. 1972. A practical algorithm for the determination of the phase from image and diffraction plane pictures. *Optik* 35: 237–246.

Gillet, J. M., and P. Cortona. 1999. Analysis of the MgO structure factors. *Phys. Rev. B* 60:8569–8574.

Goldberg, D. E. 1997. *Genetic algorithmns in search, optimization and machine learning*. Massachusetts: Addison Wesley Longman, Inc.

Granqvist, C. G., E. Avendano, and A. Azens. 2003. Electrochromic coatings and devices: survey of some recent advances. *Thin Solid Films* 442:201–211.

Grozea, D., E. Bengu, and L. D. Marks. 2000. Surface phase diagrams for the Ag-Ge(111) and Au-Si(111) systems. *Surf. Sci.* 461:23–30.

Hamnett, A., and J. B. Goodenough. 1984. *Physics of non-tetrahedrally bonded compounds*. Berlin: Springer.

Henrich, V. E. 1976. Thermal faceting of (110) and (111) surfaces of MgO. *Surf. Sci.* 57:385–392.

———. 1983. The nature of transition metal oxide surfaces. *Prog. Surf. Sci.* 44: 175–199.

Henrich, V. E., and P. A. Cox. 1994. *The surface science of metal oxides.* Cambridge: Cambridge University Press.

Hirsch, P., A. Howie, R. B. Nicholson, D. W. Pashley, and M. J. Whelan. 1977. *Electron microscopy of thin crystals.* New York: Robert E. Krieger publishing co., Inc.

Hofer, W. A., A. J. Fisher, R. A. Wolkow, and P. Grutter. 2001. Surface relaxations, current enhancements, and absolute distances in high resolution scanning tunneling microcopy. *Phys. Rev. Lett.* 87:236104.

Hotovy, I., V. Rehacek, P. Siliciano, S. Capone, and L. Spiess. 2002. Sensing characteristics of NiO thin films as NO_2 gas sensor. *Thin Solid Films* 418:9–15.

Hsu, W. Y., and R. Raj. 1992. Mgo epitaxial thin-films on (100) GaAs as a substrate for the growth of oriented $PbTiO_3$. *Appl. Phys. Lett.* 60:3105–3107.

Jayaram, G. 1995. Phd dissertation, Northwestern University .

Jeong, H.-C., and E. D. Williams. 1999. Steps on surfaces: experiment and theory. *Surf. Sci. Rep.* 34:175–294.

Johnson, D. A. 1982. *Some thermodynamic aspects of inorganic chemistry.* Cambridge: Cambridge University Press.

Keating, P. N. 1966. Effect of invariance requirements on the elastic strain energy of crystals with application to the diamond structure. *Phys. Rev.* 145:637–645.

Kim, M. Y., J. M. Zuo, and J. C. H. Spence. 1998. Ab-initio LDA calculations of the mean coulomb potential $V_\circ$ in slabs of crystalline Si, Ge and MgO. *Phys. Stat. Sol.* 166:445–451.

Ködderitzsch, D., W. Hergert, W. M. Temmerman, Z. Szotek, A. Ernst, and H. Winter. 2002. Exchange interactions in NiO and at the NiO(100) surface. *Phys. Rev. B* 66:064434.

Kresse, G., and J. Furtmuller. 1996a. Efficiency of ab-initio total energy calculations for metals and semiconductors using a plane-wave basis set. *Comput. Mater. Sci.* 6:15–50.

———. 1996b. Efficient iterative schemes for ab initio total-energy calculations using a plane-wave basis set. *Phys. Rev. B* 54:11169–11186.

Kresse, G., and J. Hafner. 1993. Abinitio molecular-dynamics for liquid metals. *Phys. Rev. B* 47:558–561.

———. 1994a. Abinitio molecular-dynamics simulation of the liquid-metal amorphous-semiconductor transition in germanium. *Phys. Rev. B* 49:14251–14269.

———. 1994b. Norm-conserving and ultrasoft pseudopotentials for first-row and transition elements. *J. Phys.: Cond. Mat.* 6:8245–8257.

Kumpf, C., L. D. Marks, D. Ellis, D. Smilgies, E. Landemark, M. Nielsen, R. Feidenhans'l, J. Zegenhagen, O. Bunk, J. H. Zeysing, Y. Su, and R. L. Johnson. 2001a. Subsurface dimerization in III–V semiconductor (001) surfaces. *Phys. Rev. Lett.* 86:3586–3589.

Kumpf, C., D. Smilgies, E. Landemark, M. Nielsen, R. Feidenhans'l, O. Bunk, J. H. Zeysing, Y. Su, R. L. Johnson, L. Cao, J. Zegenhagen, B. O. Fimland, L. D. Marks, and D. Ellis. 2001b. Structure of metal-rich (001) surfaces of III–V

compound semiconductors. *Phys. Rev. B* 64:075307.

Landree, E., C. Collazo-Davila, and L. D. Marks. 1997. Multi-solution genetic algorithm approach to surface structure determination using direct methods. *Acta Cryatallogr. B* 53:916–922.

Lawrence, J. L. 1973. Debye-waller factors for magnesium oxide. *Acta Crystallogr. A* 29:94–95.

Lazarov, V. K., S. A. Chambers, and M. Gajdardziska-Josifovska. 2003. Polar oxide interface stabilization by formation of metallic nanocrystals. *Phys. Rev. Lett.* 90:216108.

Lee, S. G., S. Lee, and H. I. Lee. 2001. Photocatalytic production of hydrogen from aquaeous solution containing CN^- as a hole scavenger. *Applied Catalysis A* 207:173–181.

Löwdin, P. O. 1953. Approximate formulas for many-center integrals in the theory of molecules and crystals. *J. Chem. Phys* 21:374–380.

Magkoev, T. T., G. G. Vladimirov, D. Remar, and A. M. C. Moutinho. 2002. Comparative study of metal adsorption on the metal and the oxide surfaces. *Solid State Commun.* 122:341–346.

Marathe, V. R., S. Lauer, and A. X. Trautwein. 1983. Electrostatic potentials using direct-lattice summations. *Phys. Rev. B* 27:5162–5165.

Marchenko, V. I. 1981. Possible structures and phase-transitions on the surface of crystals. *JETP Lett.* 33:381–383.

Marks, L. D. 1999. General solution for three-dimensional surface structures using direct methods. *Phys. Rev. B* 60:2771–2780.

Marks, L. D., C. Collazo-Davila E. Bengu, E. Landree D. Grozea, C. Leslie, and W.Sinkler. 1998. Direct methods for surfaces. *Surf. Rev. Lett.* 5:1087–1106.

Marks, L. D., N. Erdman, and A. Subramanian. 2001a. Crystallographic direct methods for surfaces. *J. Phys. Cond. Mat.* 13:10677–10687.

———. 2001b. Crystallographic direct methods for surfaces. *J. Phys: Cond. Mat.* 13:10677–10687.

Marks, L. D., M. Kubozoe, M. Tomita, M. Ukiana, T. Furutsu, I. Matsui, and F. Nagata. 1988. Design and initial performance of a U-V-HREM. *Inst. Phys. Conf. Series* 93:163–164.

Marks, L. D., and R. Plass. 1995. Atomic structure of Si(111)-(5x2)-Au from high-resolution electron-microscopy. *Phys. Rev. Lett.* 75:2172–2175.

Matsunaga, H., H. Ohno, Y. Okamoto, and Y. Nakajima. 1990. Heteroepitaxial growth of $LiNbO_3$ single-crystal films by ion plating method. *J. Crystal Growth* 99:630–633.

McKee, R. A., F. J. Walker, and M. F. Chisholm. 1998. Crystalline oxides on silicon: The first five monolayers. *Phys. Rev. Lett.* 81:3014–3017.

Merkle, K. L., J. R. Reddy, and C. L. Wiley. 1985. Grain boundaries in nickel monoxide. *Mater. Res. Soc. Symp. Proc.* 41:213–219.

Monkhorst, H. J., and J. D. Pack. 1976. Special points for brillouin-zone integrations. *Phys. Rev. B* 13:5188–5192.

Mott, N. F. 1974. *Metal-insulator transitions.* London: Taylor and Francis.

Mulliken, R. S. 1955. Electron population analysis on LCAO-MO molecular wave functions .1. *J. Chem. Phys* 23:1833–1840.

Nakamura, Y., Y. Kondo, J. Nakamura, and S. Watanabe. 2001. STM images apparently corresponding to a stable structure: Considerable fluctuation of a phase boundary of the Si(111)-($\sqrt{3}$x$\sqrt{3}$)-Ag surface. *Phys. Rev. Lett.* 87:156102.

Onishi, H., C. Egawa, T. Aruga, and Y. Iwasawa. 1987. Adsorption of Na atoms and oxygen-containing molecules on MgO(100) and (111). *Surf. Sci.* 191:479–491.

Pashley, M. D. 1989. Electron counting model and its application to island structures on molecular-beam epitaxy grown GaAs(001) and ZnSe(001). *Phys. Rev. B* 40:10481–10487.

Perdew, J. P. 1991. *Electronic structure of solids '91*, 11. Berlin: Akademie Verlag.

Perdew, J. P., K. Burke, and M. Ernzerhof. 1996. Generalized gradient approximation made simple. *Phys. Rev. Lett.* 77:3865–3868.

Perdew, J. P., J. A. Chevary, S. H. Vosko, K. A. Jackson, M. R. Pederson, D. J. Singh, and C. Fiolhais. 1992. Atoms, molecules, solids and surfaces - applications of the generalized gradient approximation for exchange and correlation. *Phys.Rev. B* 46:6671–6687.

Plass, R., K. Egan, C. Collazo-Davila, D. Grozea, E. Landree, Marks L. D, and M. Gajdardziska-Josifovska. 1998a. Cyclic ozone identified in magnesium oxide (111) surface reconstructions. *Phys. Rev. Lett.* 81:4891–4894.

Plass, R., J. Feller, and M. Gajdardziska-Josifovska. 1998b. Morphology of MgO(111) surfaces: artifacts associated with the faceting of polar oxide surfaces into neutral surfaces. *Surf. Sci.* 414:26–37.

Prusseit, W., S. Corsepius, F. Baudenbacher, K. Hirata, P. Berberich, and H. Kinder. 1992. Epitaxial growth of $YBa_2Cu_3O_7$ films on GaAs with MgO buffer layers. *Appl. Phys. Lett.* 61:1841–1843.

Renaud, G. 1998. Oxide surfaces and metal/oxide interfaces studied by grazing incidence x-ray scattering. *Surf. Sci. Rep.* 32:1–90.

Rez, D., P. Rez, and I. Grant. 1994. Dirac-Fock calculations of x-ray scattering factors and contributions to the mean inner potential for electron scattering. *Acta Crystallogr. A* 50:481–497.

Robinson, I. K., W. K. Waskiewicz, P. H. Fuoss, and L. J. Norton. 1988. Observation of strain in the Si(111) 7x7 surface. *Phys. Rev. B* 37:4325–4328.

Roth, W. L. 1958. Magnetic structures of MnO, FeO, CoO and NiO. *Phys. Rev.* 110:1333–1341.

Sanger, P. L. 1969. An experimental determination of ionic state of MgO by single crystal methods. *Acta Crystallogr. A* 25:694–702.

Sawatzky, G. A., and J. W. Allen. 1984. Magnitude and origin of the band-gap in NiO. *Phys. Rev. Lett.* 53:2339–2342.

Seminario, J. M., C. De La Cruz, P. A. Derosa, and L. M. Yan. 2004a. Nanometer-size conducting and insulating molecular devices. *J. Phys. Chem. B* 108:17879–17885.

Seminario, J. M., P. A. Derosa, L. E. Cordova, and B. H. Bozard. 2004b. A molecular device operating at terahertz frequencies: Theoretical simulations. *IEEE T. Nanotechnol.* 3:215–218.

Shashkov, D. A., and D. N. Seidman. 1995. Atomic scale studies of segregation at ceramic/metal heterophase interfaces. *Phys. Rev. Lett.* 75:268–271.

Shenoy, V. B., Shiwei Zhang, and W. F. Saam. 1998. Bunching transitions on vicinal surfaces and quantum n-mers. *Phys. Rev. Lett.* 81:3475–3478.

Sinfelt, J. H. 1986. Influence of technology on catalytic science. *Ind. Eng. Chem. Fundam.* 25:2–9.

Sinkler, W., and L. D. Marks. 1999. Dynamical direct methods for everyone. *Ultramicroscopy* 75:251–268.

Soeya, S., S. Nakamura, T. Imagawa, and S. Narishige. 1995. Rotational hysteresis loss study on exchange-coupled $Ni_{81}Fe_{19}$/NiO films. *J. Appl. Phys.* 77:5838–5842.

Sorensen, O. T. 1981. *Non-stoichiometric oxides.* New York: Academic Press.

Srolovitz, D. J., and S. A. Safran. 1986. Capillary instabilities in thin films. I.energetics. *J. Appl. Phys.* 60:247–254.

Stewart, R. F. 1973. Electron population analysis with generalized x-ray strcuture factors - higher multipoles. *J. Chem. Phys.* 58:1668–1676.

Su, Z. W., and P. Coppens. 1998. Nonlinear least-squares fitting of numerical relativistic atomic wave functions by a linear combination of Slater-type functions for atoms Z=1-36. *Acta Cryatallogr. A* 54:646–652.

Subramanian, A., and L. D. Marks. 2005. In preparation .

Subramanian, A., L. D. Marks, O. Warschkow, and D. E. Ellis. 2004. Direct observation of charge transfer at a MgO(111) surface. *Phys. Rev. Lett.* 92:026101:1–4.

Tanishiro, Y., and K. Takayanagi. 1989. Validity of the kinematical approximation in transmission electron diffraction for analysis of surface structures. *Ultramicroscopy* 27:1–8.

Tasker, P. W. 1979. The stability of ionic crystal surfaces. *J. Phys. C* 12:4977–4984.

Terakura, K., A. R. Williams, T. Oguchi, and J. Kubler. 1984. Transition-metal monoxides - band or mott insulators. *Phys. Rev. Lett.* 40:1830–1833.

Teresa, J. M. De, A. Barthelemy, A. Fert, J. P. Contour, F. Montaigne, and P. Seneor. 1999. Role of metal-oxide interface in determining the spin polarization of magnetic tunnel junctions. *Science* 286:507–509.

Tomashpolskii, Y. Y., E. N. Lubnin, M. A. Sevostyanov, and V. I. Kukuev. 1981. Structure of crystal surfaces of complex oxides (100) $BaTiO_3$, (100), (110) $SrTiO_3$ between room temperature and 1200° C. *Sov. Phys. Crystallogr.* 27: 691–694.

Tonouchi, M., Y. Sakaguchi, and T. Kobayashi. 1987. Epitaxial growth of NBN on an ultrathin MgO semiconductor system. *J. Appl. Phys.* 62:961–966.

Towler, M. D., N. L. Allan, N. M. Harrison, V. R. Saunders, W. C. Mackrodt, , and E. Apra. 1994. Ab initio study of MnO and NiO. *Phys. Rev. B* 50:5041–5054.

Tseng, M. Z., W. N. Jiang, and E.L. Hu. 1994. Measurements and analysis of hall-effect of a 2-dimensional electron-gas in the close proximity of a superconducting

$YBa_2Cu_3O_{7-x}$ film. *J. Appl. Phys.* 76:3562–3565.

Tsukada, M., H. Adachi, and C. Satoko. 1983. Theory of electronic-structure of oxide surfaces. *Prog. Surf. Sci.* 14:113–173.

Twesten, R. D., and J. M. Gibson. 1994. Kinematic analysis of transmission electron diffraction data from Si(111) - 7x7. *Ultramicroscopy* 53:223–235.

Vanderbilt, D. 1990. Soft self-consistent pseudopotentials in a generalized eigenvalue formalism. *Phys. Rev. B* 41:7892–7895.

Ventrice, C. A., Th. Bertrams, H. Hannemann, A. Brodde, and H. Neddermeyer. 1994. Stable reconstruction of the polar (111) surface of NiO on Au(111). *Phys. Rev. B* 49:5773–5776.

Wang, F., S. Muller, and R. Wordenweber. 1993. Large-area epitaxial MgO buffer layers on sapphire substrates for Y-Ba-Cu-O film deposition. *Thin Solid Films* 232:232–236.

Wang, Y., and L. D. Marks. In preparation .

Warschkow, O., M. Asta, N. Erdman, K. R. Poeppelmeier, D. E. Ellis, and L. D. Marks. 2004. TiO_2-rich reconstructions of $SrTiO_3$(001): a theoretical study of structural patterns. *Surf. Sci.* 573:446–456.

Watson, R. E. 1958. Analytic Hartree-Fock solutions for O^{2-}. *Phys. Rev.* 111: 1108–1110.

Widjaja, E. J., and L. D. Marks. 2003. Epitaxial decagonal thin films on crystalline substrates. *Phil. Mag. Lett.* 83:47–55.

Wolf, D. 1992. Reconstruction of NaCl surfaces from a dipolar solution to the Madelung problem. *Phys. Rev. Lett.* 68:3315–3318.

Wong, H., P. W. Voorhees, M. J. Miksis, and S. H. Davis. 2000. Periodic mass shedding of a retracting solid film step. *Acta. Mater.* 48:1719–1728.

Xu, P., G. Jayaram, and L. D. Marks. Cross-correlation method for intensity measurement of transmission electron-diffraction patterns. *Ultramicroscopy* 53: 15–18.

Xu, P., and L. D. Marks. 1992. Intensities of surface diffraction spots in plan view. *Ultramicroscopy* 45:155–157.

Yoon, M., S. G. J. Moochrie, D. M. Zehner, G. M. Watson, and D. Gibbs. 1994. Faceting and the orientational phase diagram of stepped Pt(001) surfaces. *Phys. Rev. B* 49:16702–16720.

Zuo, J. K., T. Zhang, J. F. Wendelken, and D. M. Zehner. 2001. Step bunching on TaC(910) due to attractive step-step interactions. *Phys. Rev. B* 63:033404.

Zuo, J. M., P. Blaha, and K. Schwarz. 1997a. The theoretical charge density of silicon: Experimental testing of exchange and correlation potentials. *J. Phys: Cond. Mat.* 9:7541–7561.

Zuo, J. M., M. O'Keeffe, and J. C. H. Spence. 1997b. Charge density of MgO: Implications of precise new measurements for theory. *Phys. Rev. Lett.* 78:4777–4780.

Zuo, J. M., J. C. H. Spence, and M. O'Keeffe. 1988. Bonding in GaAs. *Phys. Rev. Lett.* 61:353–356.